Third Year Technical Report, Part 1
NGR 23-004-091
NASA Lewis Research Center
Grant Number 23-004-068

MEASUREMENTS IN A LARGE ANGLE OBLIQUE JET IMPINGEMENT FLOW

prepared by

John F. Foss, Associate Professor

Division of Engineering Research
MICHIGAN STATE UNIVERSITY
East Lansing, Michigan 48823

Third Year Technical Report, Part 1
NGR 23-004-091
NASA Lewis Research Center
Grant Number 23-004-068

MEASUREMENTS IN A LARGE ANGLE OBLIQUE JET IMPINGEMENT FLOW

prepared by

John F. Foss, Associate Professor

Division of Engineering Research
MICHIGAN STATE UNIVERSITY
East Lansing, Michigan 48823
January, 1974

ABSTRACT

Velocity and surface pressure measurements, in the flow field of an obliquely impinging jet, and their interpretation as regards the governing mechanics and the aerodynamic noise generation characteristics of such a flow are reported. A computer controlled probe positioning mechanism allowed the measurement of the velocity magnitude and direction in the plane parallel to the plate. The mean velocity and Reynolds stress components were recorded. Measures of the terms in the momentum equation reveal the character of the pressure gradients in the neighborhood of the stagnation point. The effects of the stagnation streamline location on the vorticity field and the "Vortex Sound" considerations of Powell [12] are discussed in relationship to the aerodynamic noise generation effects of this flow.

TABLE OF CONTENTS

NOMENCLATURE

d	nozzle diameter, 1.9 cm (0.75 in) for the present study
e	hot-wire voltage signal
k	curvature of the jet centerline
p	static pressure
r, θ, z	cylindrical coordinates (see Figure 2)
u_r, v_θ, w	velocity components* in the r, θ, z directions
u_o	inviscid velocity magnitude at the exit of the jet
$\underset{\sim}{V}$	velocity vector
x, y, z	cartesian coordinates (see Figure 2)

Greek Symbols

α	inclination of the approach jet (see Figure 2)
β, β_o	angle of the probe, angle of the streamline respectively, with respect to the radial direction
$\Delta ( )$	difference of ( )
∇	del (nabla) operator
ν	kinematic viscosity
ρ	density
$\underset{\sim}{\omega}$	vorticity vector

Superscripts

$\bar{( )}$	time average

*Note, lower case velocity components signify both the mean and fluctuating velocity components as designated by the superscript.

1. INTRODUCTION

1.1. Motivation

The successful development of STOL aircraft requires large lift forces at relatively low forward aircraft speeds. The proposed utilization of these aircraft will be to service airports near urban population centers; hence, it is important that this lift augmentation be effected with a sufficiently quiet propulsion scheme. The externally blown flap (e.b.f.) represents one of several configurations under consideration by the National Aeronautics and Space Administration to achieve the required low speed lift characteristics; however, it has also been determined that considerable acoustic noise can be generated by the jet impingement flow field associated with this configuration. The e.b.f. configuration and the oblique jet impingement flow as its laboratory or fundamental counterpart are shown in Figure 1. Identification of the sources of this noise and the development of techniques to limit it can best be achieved by a multi-faceted research program. Numerous studies by National Aeronautics and Space Administration personnel and other researchers (a representative sample is provided by references 1-4) have demonstrated characteristic features of the acoustic generation. The research project described herein is motivated by a different aspect of the problem. Specifically, it is proposed to investigate and identify the basic mechanics of the oblique jet impingement flow field. The pressure and turbulent stress fluctuations, which are responsible for the acoustic noise, result from the dynamics of the jet impingement flow. Although the relationship of the acoustic noise generation to these fluid dynamic quantities is quite subtle and complex, a knowledge of the mean flow, the turbulent stresses and the vorticity characteristics will provide pertinent background for theoretical studies of the acoustic characteristics of the e.b.f. Similarly, the aerodynamic considerations of achieving an attached flow on the suction side of the flap require a knowledge of both the large and small angle jet impingement flows as the background information to adequately describe the flow through the flap gap.

1.2. Oblique Jet Impingement

The mechanics of the shallow angle, oblique jet impingement flow field have been successfully inferred from comprehensive pressure and velocity measurements by Foss and Kleis [5]. A summary of these

results is presented below and the relationship to the present work is also noted.

The presence of the plate imposes a kinematic constraint on the jet flow; namely, the material of the jet cannot penetrate the plane of the impact surface. This requires that the jet curve upward to flow over the plate and/or that it spread laterally over the plane of the surface. Normal jet impingement involves only the latter response; the results of [5] indicate that the jet response is primarily an upward curvature for small angles ($0 \leq \alpha \lesssim 12$ degrees, see Figure 2 for the nomenclature). This inferrence is made possible by comparing the surface pressure isobars with a reference curve. The zero isobar curve and the contour which represents the intersection of the $0.1u_o$ isotach (u_o = jet exit velocity) and an imaginary plane located at the plate's surface are proportional in width for the small angle cases. Since the zero isobar contour is a measure of the dynamically significant jet width, this proportionality is interpreted as an absence of significant jet spreading.

An analytical development is presented in [5] which allows the curvature K of the jet center* z_m to be determined from the surface pressure measurements. The curvature of the jet K(x) results from the net effect of the pressure up to that x location; hence, it depends upon the lateral as well as the longitudinal pressure distribution. It is possible to compare the K(x) distribution with the centerline pressure distribution p(r,0,0) and determine a measure of the equilibrium between the centerline and the total pressure conditions. This comparison demonstrates the relative effect of the two geometric parameters, specifically, the impingement angle and the distance from the plate. By comparing the spreading measures with the K(x) vs p(r,0,0) measure it is possible to infer that 1) the small angle and small distance above the plate condition does not demonstrate significant spreading but neither is the central portion of the flow in equilibrium,** 2) the large angle flows show systematic spreading and a lack of equilibrium, and 3) the other two combinations are observed for intermediate angles and displacements.

* $r,0,z_m$ is the location of the vector which is the mechanical equivalent of the jet's momentum flux.

** The concept of equilibrium in this context is more descriptive than quantitative. Specifically, it refers to the relative trends between the maxima of the p(x,o,o) and k(x) curves and, in addition, the general shape of the curves. The word equilibrium is to connote whether the jet turns em-masse or whether the center plane phenomena as revealed by p(x, o, o) is significantly different from the turning of the entire jet as revealed by the K(x) curve.

A comprehensive argument is formulated in [5] which demonstrates that vorticity effects are of primary significance in the mechanics of the oblique impingement flow. The flow through a plane normal to the streamwise flow is considered to represent the effects of vorticity transport of the original azimuthal vorticity of the approach jet, the production of vorticity by the stretching and reorientation of the mean velocity field and the flux of vorticity through the plane of the surface. (The latter is a consequence of the surface pressure gradients.) The overall details of this model will not be considered here, the reader is referred to [5]; also, the vorticity effects which are pertinent to the acoustics problem are discussed by Foss [6] in a paper which is also reproduced in Appendix B of the Third Annual and Final Report describing the total research program supported by Grant No. NGR 23-004-068.

The mechanics of the large angle impingement flow are more complicated than those for the shallow angle cases reported in [5]; however, many aspects of, and the basic framework for, the analysis can be used from this earlier study. In addition, some relevant experimental data is available from Donaldson and Snedecker [7] and Westley, et. al. [8]. Funk [9] has made use of prior analytical work to interpret the noise producing mechanism of the e.b.f. configuration. His interpretation of the "scrubbing mechanism" is of particular interest and is discussed in a later section. Beyond this, there are no additions to the earlier literature review presented by Foss and Kleis [10]. It should be noted that support for this work has been obtained from the NASA Langley Research Center, Noise Control Section, Dr. Jay Hardin, Grant Monitor, Grant No. NGR 23-004-091.

2. EXPERIMENTAL FACILITY

2.1. Flow System

A schematic of the laboratory utilized for this study is shown in Figure 3. A large centrifugal fan (speed control to $\pm$ one percent) with an induced flow 7.5 in. pipe test section and a large plenum chamber on the pressure side is available for this work. The 105 diameter long pipe is used to evaluate the performance of the hot wire data acquisition

system by comparison with the universal fully-developed pipe flow results of Laufer [11] and by the absolute evaluation of the Reynolds stress term ($-\rho \overline{u}\overline{v}$) from its linear variation with respect to radius and its magnitude as determined from the pressure gradient in the pipe. Such a procedure is used to determine the precise (and operationally defined) angle between the two wires of an x-wire array. Such an evaluation scheme is described by Patel [12]. The oblique impingement flow system is shown in Figure 4; a flexible duct connects the plenum chamber to the large diameter inlet tube shown in the figure.

The design of the oblique jet impingement flow system was controlled by several primary contraints. The ability to position the probe at any r, θ, z location and the ability to align the probe with the mean velocity orientation in the r, θ plane were considered essential. The latter constraint preserves the accuracy of the calibration, for small pitch angles, since the probe is calibrated at zero yaw angle to the flow. A traverse system, mounted on a lathe bed carriage, with computer controlled stepping motor drives is available; it was decided that this unit would be used for the large angle oblique impingement flows. This unit is capable of positioning the probe to within 0.001 in. perpendicular to the lathe bed, to within 0.001 in. in z and to within 0.5 degrees in the r,Θ plane. The desired range of Θ values could only be accounted for by a relative angular motion of the jet with respect to the lathe bed. This has been accomplished by mounting the jet on a rotating support such that its axis passes through (0,0,0) at an angle of $\pi/4$ radians with respect to the vertical axis. The probe traverse system also required the gear box and stepping motors to be located directly below the measuring point; hence, the probe is supported on a U shaped holder. The "length of the U" is restricted by vibration and structural stiffness constraints; a value of 12 inches was arbitrarily selected for this off-set distance. Consequently, the impact plate is in the form of a circular arc with a radius of 10 inches from the "impact point" (0,0,0) to the plate edge. A jet nozzle of 0.75 in. internal diameter was selected as a nominal size to allow sufficiently large r/d values, before the plate edge influences the data, and sufficient resolution for the z/d region of interest.

2.2. Data Acquisition System and Measurement Techniques

A Texas Instruments 960 A minicomputer is the central component in the data acquisition system (see Figure 5). This unit is used to position the probe at the r, z values prescribed for the traverse (e.g., 13 data points at $z = 0.05$ d, $0 \leq r \leq 4$ in.) by means of analog voltage signals used to drive the stepping motors, to record the data for a prescribed time period (e.g., 60 second averaging time) and to orient the probe into the mean flow direction of the r, Θ plane by a scheme which relies upon the symmetric and approximately cosine response of a yawed hot-wire probe. The probe is positioned at $\pm$ 45, $\pm$ 30, $\pm$ 15, and 0 degrees with respect to the presumed flow direction (the direction found in the previous reading of the traverse), and the streaming direction (β_o) is calculated by the following technique. The mean hot-wire response at each of the seven positions $\overline{E}_i$ (β_i), is divided by the maximum voltage $\overline{E}_{max}$, and the apparant angle of the probe with respect to the head-on condition ($\beta_i - \beta_{oi}$) is calculated from the relationship

$$\frac{\overline{E}_i}{\overline{E}_{max}} = \cos(\beta_i - \beta_{oi}). \qquad (1)$$

The voltage values from the hot-wire probe (or static pressure transducer) are digitized and initially processed in the minicomputer such that subsequent processing will result in the mean velocity and turbulence quantities expressed in laboratory coordinates, viz., $\overline{u_r}$, $\overline{u_\theta}$, $\overline{u_r^2}$, $\overline{u_\theta^2}$, $\overline{u_r u_\theta}$. Specifically, let e_o, e_1, and e_2 be voltage values from the hot-wire probe as it is oriented at β_o and at $\beta_o \pm 45$ degrees respectively.

$$\overline{f(e_k)} = \frac{1}{N} \sum_{j=1}^{N} [f(e_k)]_j \qquad (2)$$

where j is one sample of the digitized record (the digitized values are formed at the rate of 20 khz) and N is dependent upon the sampling time, e.g. $N = 6 \times 10^5$ for a 30 second sample. $f(e_k) = e_o, e_1, e_2, e_o^2, e_1^2, e_2^2$. These values are recorded for specified traverses until sufficient information is recorded; the averaged values are then transferred to the IBM 1800 computer where the voltages are converted to velocities via the response equations of the wires and the fourth order polynomial used

to fit the calibration, $e = e(u)$, of the "linearized" hot-wire probes. Two mean velocity and three Reynolds stress terms are known at the given point in terms of probe coordinates (s,t,z). The data can then be transformed to (r,Θ,z) coordinates.

3. THE PRESENT INVESTIGATION

3.1. Motivation and Scope

The motivation for the present study reported herein is the aforementioned acoustic and aerodynamic effects associated with the externally blown flap. The relationship of this application problem to the oblique impingement of a single axisymmetric jet on a large plane surface, the lack of detailed information describing the mechanics of the latter flow field and the assessment that an appropriate initial study would encompass detailed radial velocity traverses with selected vertical traverses established the scope of the present investigation. The results, presented below, support this assessment of an appropriate scope for the investigation. That is, sufficient information is now available that a comprehensive program can be identified to examine the appropriate details of the large angle impingement flow field. The suggestions for future studies are presented in the final section of this report.

3.2. Results

There are two principal categories of results derived from the data of the present study; these are i) documentation of the flow field and ii) characteristics of the flow field as inferred in the available data. These two results will be separately presented and discussed.

3.2.1. Documentation

The data representing the time mean surface pressure field measurements have been collectively presented in the form of surface isobars; these are shown on Figure 6 (a). An expanded scale to better delineate the maximum pressure region is used in Figure 6 (b). The length from the jet exit to the impact plate was seven diameters and the impingement angle was $\pi/4$ radians. These are the conditions for all of the data reported herein.

The velocity field information was collected in three separate series of data acquisition runs. Single wire and fixed orientation traverses were made in the jet prior to its impact on the plate and also

downstream of the geometric impact point. These data are shown in Figure 7 . These results indicated that a local maxima in the velocity occured near $z/d = 0.053$ ($z = 0.04$ in.). Hence, this elevation was selected as the location of the plane for the radial traverses to define the velocity field near the plate. A composite view of this velocity field is presented in Figure 8 . The vertical velocity traverses to complete the exploratory documentation were taken at $r/d = 1$ and $r/d = 3$ and at the angles $\theta = \pi/4$ and $\pi/2$. These results are presented in Figure 9 . In addition to the graphical presentation, a listing of the data is provided in Appendix A. As discussed below, there is reason to suspect the detailed values from the $\pi/3$ and $\pi/6$ radial traverses. Hence, these have been excluded from the listing even though they are considered to be sufficiently accurate to be included in the composite plot of Figure 8 .

In order to complete the graphical documentation of the radial velocity traverses, it was decided to adopt a presentation format which would allow the relative importance of the various turbulence kinetic energy production terms to be assessed. These data are shown in Figures 10 to 13. Since the radial traverses were taken in even increments ($\Delta r/d = 2/3$) it is possible to construct both radial and azimuthal plots of the radial and azimuthal mean velocities, fluctuating velocity intensities and fluctuating velocity correlation (kinematic Reynolds stress).

In order to facilitate the comparison of the production effects, the vertical ordinates were essentially maintained at constant values for all plots. The abscissa scale for the radial traverse presentations was kept constant for all plots but is a more expanded scale than that used for the azimuthal plots. The abscissa length is contracted approximately 50 percent for the azimuthal plots. Hence, the gradients appear to be too large by this factor. An additional radial traverse which makes use of a somewhat finer series of probe locations and which is slightly closer to the plate is presented in Figure 14.

The azimuthal plots of the radial traverse data revealed apparant inconsistancies from the $\Theta = \pi/3$ and $\pi/6$ runs. Consequently, these data were removed from Figures 10 to 13 and the data listings of Appendix A. They were utilized in the more pictoral representation of the velocity field presented in Figure 8.

3.2.2. Characteristics of the Large Angle Impingement Flow Field

There are two principal characteristics of the large angle impingement flow which have been deduced from the data base represented by the results discussed above. The first characteristic is that the flow field near the plate demonstrates two distinct "symmetry"* patterns, one is "centered" near the location of the maximum surface pressure and the second is a symmetry pattern about the geometric intersection of the jet axis with the plate and is realized when the flow reaches a sufficiently large radial distance. The second characteristic is that the turbulence kinetic energy in the region above the plate is not significantly greater than that which can be accounted for by the convection of turbulence energy by the mean motion. The data which allow the inference of these two characteristics and their significance for the generation of acoustic noise and the aerodynamic phenomena of the externally blown flap configuration are examined in subsequent sections.

3.2.2.1. Symmetry Characteristics of the Flow near the Surface

An overall picture of the flow pattern near the surface of the plate is provided by combining the data from all of the radial traverses in such a manner that the magnitude and direction of the velocity in the $z/d = 0.053$ plane is revealed. This plot is presented in Figure 8 .

The symmetry "point" for the neighborhood of the maximum pressure is approximately $r/d = 0.87$ (see Figure 6 (b)) and a "local symmetry" of the $\chi(r,\theta)$ field about this location is suggested by the data of the composite plot. Considerably more data in this region and a more sophisticated measurement technique, which is capable of segregating the r, θ, and z velocity components, would be required to improve the quantitative assessment of this flow pattern. The qualitative observation of local symmetry around the maximum pressure region is expected to be supported by these additional measurements. As described in a subsequent section, the present study was not extended to include these measurements since a major modification to the flow and instrumentation system is projected for the continuation study.

For sufficiently large r values ($r/d \approx 3$ which represents an r/z value of approximately 55) the flow pattern near the surface evolves

* The word "symmetry" is not meant to imply azimuthal independence of the velocity fields, e.g., at a given r, $\overline{u}_r(o) > \overline{u}_r(\pi)$. The "symmetry point" is rather like a non-axisymmetric source location.

such that the geometric intersection of the jet axis and the plate is the symmetry "point". The radial traverse data for $\overline{v}_\theta/u_o$ (see Figure 11) demonstrates this effect quantitatively and the vanishing $\overline{u_r v_\theta}$ values (see Figure 12) from the same traverses similarly confirm this observation. The azimuthal variation of $\overline{u}_r/u_o$ (see Figure 12) shows that the flow is not axisymmetric about the symmetry point (this is not an expected result since the jet inclination is $\pi/4$, not $\pi/2$ radians with respect to the plate) but these distributions also show that the variation with respect to θ becomes rather slight as r increases. It is important to recall that these results are for the region quite close to the plate. The flow at a sufficient elevation above the plate will retain its predominant $\theta \approx 0$ orientation. The surface velocity pattern is corroborated by the visualization studies of Westley, etc. al. [8].

The governing mechanics which result in these symmetry patterns are not fully revealed by these data. Without direct measurements of $\overline{w}(r,\theta)$ and $\overline{u_r w_z}$ and considerably more comprehensive data, such an assessment would not be feasible. However, the local symmetry about the maximum pressure strongly suggests that the pressure gradient is the dominant term in the equation of motion for this region of the flow. Some quantitative evaluations made possible by the extant data confirm this speculation. These are presented in Section 3.2.3.

The effects which lead to symmetry about the geometric origin are much more obscure. The surface static pressure field is clearly not symmetric about the origin and this would suggest that the local effects leading to such symmetry are the Reynolds stresses, i.e., $\overline{u_r v_\theta}$ and $\overline{v}_\theta^2$. It seems clear that the global symmetry of the entire jet is involved in the processes which lead to this result. However it is not a simple matter to connect the global effects to the Reynolds stresses which must be responsible for the local accelerations required to give the observed symmetry. One mechanistic feature of the jet which has the potential for such an effect is the predominant azimuthal vorticity of the approaching jet.

3.2.2.2. *The Turbulence Field near the Plate Surface*

The presence of the plate with the consequent no slip condition and the strong velocity gradients might lead to the apriori expectation that the turbulence energy level near the plate is substantially greater than that to be expected if the plate were absent. This expectation is not supported by the data. Also, this observation is relevant to the "scrubbing mechanism" discussed by Fink [9].

Figure 15 has been prepared as a composite plot of the turbulence intensity information from the radial traverses. In order to compare the turbulence levels near the plate with the turbulence level of the jet itself, the data for the condition $z/d = 0.053$ and $\theta = 90$ degrees has been plotted on the same figure with the radial traverse data of $x/d = 6$ and 8, from Kleis and Foss [13], see Figure 16. This comparison appears to be the most reasonable basis from which to evaluate the relative turbulence level created by the impingement process given the available experimental data. However, it is not unambiguous. A preferrable comparison would be on the basis of a volume integral of the turbulence energy in a given streamwise domain. Such an integral could be readily formulated for the axisymmetric case but would require an extensive series of traverses in the three-dimensional impingement flow. The vertical traverse data of Figure 9 show that the turbulence intensity magnitudes in the plane $z/d = 0.053$ is representative of the maximum values for these quantities in the impingement flow albeit there is a slight increase in the steep gradient $(\partial \overline{u}_r/\partial z)$ region for $z < 0.053d$. For the present, the observation that there is not a significant excess of turbulence kinetic energy will be used as a guiding characteristic and the enhanced production of acoustic energy will be sought in terms of other sources of sound generation. This is discussed in a later section.

The suppression of the turbulence intensity and the Reynolds stresses by concave curvature is discussed along with numerous other effects at length by Bradshaw [14]. The present observations regarding the maximum turbulence intensity values are compatible with these considerations. The r.m.s. surface pressure data of Westley, et. al. [8] indicate two maxima located up and downstream of the origin. Apparently, these are related to the stagnation point and to the local maxima in the turbulence intensity magnitudes observed in the present data.

3.2.3. Additional Characteristics of the Large Angle Oblique Jet Impingement

3.2.3.1. Stagnation Point

A technique of identifying the stagnation streamline by comparing the measured velocity near the plates surface with the surface static pressure taps was successfully employed by Foss and Kleis [5] to demonstrate that the stagnation point is considerabley upstream of the maximum pressure location and near the zero surface isobar for the

shallow angle impingement flow field. A necessary characteristic of this technique is that the static pressure at the location of the velocity measurement be equal to the atmospheric value. In the earlier study, an over-pressure at the velocity measuring location would have resulted in a farther upstream movement of the inferred stagnation point.

The same technique cannot be applied to the measurement of the stagnation point in the large angle case. This result is based upon the following observations: i) the local symmetry of the velocity field (see 3.2.2.1) requires that the stagnation point be in the neighborhood of $x/d \simeq -1$ and ii) comparing the surface pressures in this region with the dynamic pressure inferred from the jet velocity traverse of Figure 7, the static pressure at the location of the velocity measurement must be greater than zero. Specifically, from Figure 7 ,

$$p\ (r/d = 1,\ \theta = \pi) = \rho \overline{u}_o^2\ (0.2) + p_{atm} \tag{3}$$

and from Figure 6(b) the velocity magnitude in this neighborhood of the approaching jet is of the order of $0.3\ u_o$. The stagnation pressure for such a condition is given by

$$p_{stag} = p + \rho\ u_o^2\ (0.045) \tag{4}$$

Comparing the two equations, it is apparant that the static pressure at the measuring point must be of the order of $0.15\ \rho\ u_o^2$. A similar evaluation of the stagnation pressure is possible using the data of the radial traverse at $z/d = 0.053$; however, the closest data point to the suspected stagnation point is $r/d = 1.33$. The recorded value is $u = 0.179\ u_o$ and this suggests that the pressure along the stagnation streamline at this elevation is of the order $0.185\ \rho\ u_o^2$. Comparing these two approximate results supports the presumed streamwise pressure variation along the stagnation streamline.

3.2.3.2. Radial Equation of Motion

The extant data allow an examination of the terms in the radial equation of motion near the stagnation point. The pertinent equation of motion is

$$\overline{u}_r \frac{\partial \overline{u}_r}{\partial r} + \frac{\overline{v}_\theta}{r} \frac{\partial \overline{u}_r}{\partial \theta} + \overline{w} \frac{\partial \overline{u}_r}{\partial z} = -\frac{1}{\rho} \frac{\partial p}{\partial r} + \nu \nabla^2 \overline{u}_r - \left(\frac{\partial \overline{u}_r^2}{\partial r} + \frac{1}{r} \frac{\partial \overline{u_r v_\theta}}{\partial \theta} + \frac{\partial \overline{u_r w}}{\partial z} \right) \tag{5}$$

For the region in question, $\overline{v}_\theta \equiv 0$, $\partial \overline{u}_r / \partial z \approx 0$, $\nu \nabla^2 \overline{u}_r \approx 0$, and $\overline{u_r v_\theta} \approx 0$.

At $z = 0$, the pressure gradient $(\partial p/\partial x)$ and shear gradient $(\partial \tau_{rz}/\partial z)$ are in balance and it can be assumed that the latter, for $z > 0$, is less than or equal to its value at the wall.

$$\bar{u}_r/u_o \frac{\partial(\bar{u}_r/u_o)}{\partial r/d} \approx -\frac{\partial(p/\rho u_o^2)}{\partial r/d} - \frac{\partial(\bar{u}_r^2/u_o^2)}{\partial r/d} + \frac{\partial(\tau_{rz}/\rho u_o^2)}{\partial z/d} \qquad (6)$$

$$\text{-A-} \qquad \text{-B-} \qquad \text{-C-} \qquad \text{-D-}$$

The quantities A and C can be evaluated from Figure 14. They are, for $r/d = 0.667$,

$$A \approx -0.091$$

$$C \approx +0.0215$$

From the detailed isobar plot and using the arguments preceding (6), term D is approximated as

$$D \approx -0.0308$$

Consequently, using these values, the "equation" would be

$$A - C - D = B$$

$$-0.091 - 0.0215 + 0.0308 = 0.0717$$

It is inferred from this evaluation that the radial pressure gradient at $z/d = 0.04$ is much larger than the same quantity at $z = 0$. This observation suggests that the high pressure of the stagnation point region extends above the plate and that it is relatively more localized than at $z = 0$. That is, if an isobaric plot could be made at $z/d = 0.04$, then the contours would be much closer together than that shown in Figure (6b). Presumably, a similar phenomenon would be observed at larger distances from the plate.

3.3. Implications: The Production of Acoustic Noise

On the basis of the shallow angle impingement flow data, it has been previously proposed by Foss [6] that Powell's "Vortex Sound" arguments are quite relevant to the description of the noise produced by the jet-plate impingement flow. The present results not only support the same interpretation for the large angle impingement case, they also provide additional quantitative support for the relevance of such a model.

Powell [15] has shown that the similarity between the dipole effect (Δp across the surface area s, which leads to a corresponding mass flux across the plane of the surface) and the circulation Γ, which characterizes the strength of the vortex whose axis forms the contour bounding the area, can be used to develop an expression for the far field velocity $u(\underset{\sim}{x},t)$ as

$$u(\underset{\sim}{x},t) = \frac{\hat{x}}{4\pi x c_a^2} \left[\frac{d^2}{dt^2} \Gamma s\right]^*$$

where c_a is the ambient speed of sound and * signifies a delayed time. A schematic representation of this relationship is shown in Figure 17. This expression can be used to infer what properties of the vorticity in the oblique jet impingement are most important for the noise generation. It should also be noted that arguments similar to those referenced here have been used by Hardin [16] to evaluate the acoustic characteristics of the orderly structures in the turbulent jets.

As suggested by (7) the contribution to the acoustic noise is from the unsteadiness with which the vortex loops change. (The solenoidal condition $\nabla \cdot \underset{\sim}{\omega} = \nabla \cdot (\nabla \times \underset{\sim}{V}) \equiv 0$ requires that the vorticity appear in closed loops or terminate on the boundary of the flow.) The azimuthal vorticity of the approach flow will be distorted by the interaction with the plate and the surface flux of vorticity will require a modification of the vortex loop structures within the jet field. When viewed from the material coordinates of a portion of a given loop, the first time derivative of Γs can be expected to be large for those loops which are elongated by the interaction with the plate and/or for those loops in which significant migration of the loop into new fluid occurs. The contribution to $u(\underset{\sim}{x},t)$ comes from the unsteadiness (i.e., the magnitude of the turbulent fluctuations) with which this occurs. These effects are shown schematically in Figure 18.

The location of the stagnation streamline, which is important for the qualitative discussion associated with Figure 18, has been approximately identified from the surface pressure distribution and the velocity field symmetry conditions as discussed in Sections 3.2.3.1 and 3.2.2.1. This location is marked on the midplane velocity data traverse of Figure 7. From these considerations, it is obvious that a quite significant amount of the vorticity in the approach flow, i.e., those loops which are external to the $\approx 0.3u_o$ isotach cone, will be reformulated by the viscous diffusion of vorticity. The requirement that this reformulation be associated with viscous diffusion effects is discussed at length, along with similar considerations, in [6]. The diffusion effect is briefly considered here for completeness; viz., given the time mean vorticity equation for the material elements in the $\theta = o, \pi$ plane of the loop,

$$\frac{D\overline{\omega}_y}{Dt} = \underset{\sim}{\overline{\omega}} \cdot \nabla \overline{v} + \nu \nabla^2 \omega_y,$$

the only mechanism to alter the sign of ω_y is the viscous diffusion term. These effects are, of course, quite important near the stagnation point.

It appears reasonable that the quantitative magnitude of the "reformulation" contribution to the radiated sound is much greater, per unit volume of the jet fluid, than the stretching effects which will occur inside the ≈ 0.3 isotach cone. However, the total contribution to the sound field is not as easily assessed since the relative fractions of the flow in which these two effects are important is not obvious.

A detailed investigation of the stagnation region is suggested by these results. The plans for such a study are presented in the next section.

4. Suggestions for Future Studies

The brief listing of suggestions for further studies in this section is specifically related to the aerodynamic noise generation considerations which have been the main focus of this study. These suggestions, therefore, are related to, but are perhaps not identical with, the further studies which would be appropriate if the aerodynamics application was the primary motivation.

Given the previous discussion of the "vortex sound" [6, 14] considerations, two major areas of interest are easily identified, namely, i) the stretching and deformation effects of the vorticity interior to the stream surface which contains the stagnation streamline and ii) the details of the vorticity field in the neighborhood of the stagnation point and the reformulation of the axisymmetric vortex loops associated with the stagnation phenomena.

It is recommended that any experimental investigations of the former effects be coordinated with a significant analytical effort. There are two reasons for this recommendation: i) the governing equation for the bulk of the vorticity in this region is somewhat simpler than the full equation (the viscous diffusion term can be neglected) and ii) the quantity of data to provide an "unguided" documentation of this three-dimensional flow field is unreasonably large even for the computer aided acquisition capability as described in this report.

Conversely, the study of the flow field in the neighborhood of the stagnation point is quite compatible with a rather direct experimental approach. From the results of the present investigation, a new experimental

configuration is suggested in which the nozzle diameter is significantly increased to allow the velocity maxima ($z/d = 0.05$) to be physically moved away from the plate and hence to allow this region to be studied in detail. Also, the construction technique of a fixed probe traverse axis and a movable jet does not appear to be compatible with the demands for precise measurements in the stagnation point region. Hence, a fixed jet and an additional degree of freedom for the traverse device (x and y as well as z and θ) should be made available. The flow direction measurement scheme described in Section 2.2 appears quite adequate and should be retained.

Specific measurements should include data on the transverse vorticity component, namely $\omega_t = \frac{\partial w}{\partial s} - \frac{\partial u_s}{\partial z}$ which is feasible given adjacent x (vertical) and parallel (horizontal) wires to form the required derivatives. (Note that an instantaneous evaluation of the derivatives and their difference is required to examine ω_t.) The stagnation point should be examined with independent techniques such as tracers, velocity direction measurements, and wall shear stress indicators. The measurements must allow for the (supposed) unsteady and obviously strongly three-dimensional character of the stagnation region. These characteristics make this investigation much more complex than similar investigations of the stagnation region in axisymmetric or plane flows.

Finally, it would be beneficial to modify the surface pressure measuring configuration to again allow the x-y coordinate evaluation of $p(x,y,o)$. Such data can be readily processed as before, see Foss and Kleis [5], to reveal the trajectory of the jet centerline (based upon the momentum flux) and consequently the curvature of the centerline. Such an arrangement would also allow for a finer and more regular grid spacing of the measurements in the neighborhood of the stagnation point.

The examination of the governing mechanics of the oblique jet impingement can benefit from the extensive discussion by Bradshaw [14] of the mechanistic features of curvature effects on turbulence structure. Also, this serves to emphasize the complexity of the present problem. Specifically, the curvature effects near the stagnation point will influence the turbulence stress field which, along with the static pressure gradient and inertial effects, will determine the selection of the stagnation streamline. As noted by Bradshaw, the mechanics of the normal jet impingement flow are not well known. The oblique impingement flow is, of course, a much more complicated one.

5. Conclusions

The following conclusions are supported by the results of this study.

1) The plane defined by $z/d \simeq 0.05$ is in the neighborhood of the maximum velocity over most of the plate. Hence, this is also a plane separating regions of opposite sense vorticity. (Note that $\partial\overline{u}_s/\partial z >> \partial\overline{w}/\partial s$).

2) The flow in the $z/d \simeq 0.05$ plane (and presumably for smaller z/d values) can be characterized in terms of two symmetry patterns. Specifically, a local symmetry about the inferred stagnation point ($x/d \simeq 0.8$) for the near region and symmetry about the intersection of the jet axis and the plate ($r/d = 0$) for larger radius values. The latter effects are predominant for $r/d \gtrsim 3$.

3) The maximum levels of the turbulent fluctuations in the region near the plate are not larger than the turbulence levels of the approach jet. Insufficient data is available to establish whether or not the jet / plate interaction results in an increase in the total turbulence kinetic energy.

4) Vortex sound considerations in combination with the identification of the stagnation streamline in the sheared region ($\overline{u}/u_o \simeq 0.3$) suggest that vorticity considerations are quite important regarding the production of acoustic noise. The general characteristics of the impingement process suggest that the surface vorticity field and the major reorientation of the originally azimuthal vorticity field can be studied via a direct experimental approach. The study of the less intense, but more volumetrically more extensive, vorticity effects in the flow interior to the stagnation stream tube should be guided by appropriate analytical considerations.

5) Quantitative estimates of the terms in the equations of motion indicate that significant vertical and streamwise pressure gradient effects exist in the neighborhood of the stagnation point.

6. References

1. Dorsch, R.G., W.J. Kreim, and W.A. Olsen, "Externally-blown-flap noise," Paper 72-129, Jan. 1972, AIAA New York, N.Y.

2. Putnam, T.W. and P.L. Lasagna, "Externally blown flap impingement noise," AIAA Paper No. 72-664, 1972.

3. Haas, M., "Blown flap noise," MIT Report FTL 72-5, 1972.

4. Olsen, W., J. Miles, and R. Dorsch, "Noise generated by impingement of a jet upon a large flat board," TN D-7075, 1972, NASA, Cleveland, Ohio.

5. Foss, J.F. and S.J. Kleis, "The oblique impingement of an axisymmetric jet," Second Annual Report, NASA Grant NGR 23-004-068, December 21, 1972.

6. Foss, J.F., "Vorticity effects in oblique jet impingement flows as a background for the acoustics problem," Interagency Symposium on University Research in Transportation Noise, edited by G. Banerian and K. Karamcheti, Vol. I, 273, Stanford University (March 1973).

7. Donaldson, C. DuP. and R. Snedecker, "A Study of free jet impingement. Part 1. Mean properties of free and impinging jets," Journal Fluid Mechanics, Vol. 45, p. 2, 1971.

8. Westley, R., J. H. Woolley, and P. Brosseau, "Surface pressure fluctuations from jet impingement on an inclined flat plate," AGARD Sympossium on Acoustic Fatigue.

9. Fink, M. R., "Mechanisms of externally blown flap noise," AIAA Paper No. 73-1029, Oct. 1973.

10. Foss, J.F. and S.J. Kleis, "A study of the round-jet/plane-wall flow field," First Annual Report, Grant NGR 23-004-068 (October 1971).

11. Laufer, J., "The structure of turbulence in fully developed pipe flow," NACA Report No. 1174, 1954.

12. Patel, R.P., "Measurement of the Reynolds stresses in a circular pipe as a means of testing a Disa constant-temperature hot-wire anemometer," McGill University Technical Note 63-6.

13. Kleis, S.J. and J.F. Foss, "The effects of exit conditions on the development of an axisymmetric turbulent free jet," Third Year Technical Report, Grant No. NGR 23-004-068 (1974).

14. Bradshaw, P., "Effects of streamline curvature on turbulent flow," AGARDograph No. 169, August 1973.

15. Powell, A., "Theory of vortex sound," Journal Acoustical Soc. of Am., 36, 1, 177-195, January 1964.

16. Hardin, J. C., "Analysis of noise produced by an orderly structure of turbulent jets," NASA TN D-7242, April 1973.

RADIAL TRAVERSE JET AT 0 DEGREES

r/d	z/d	β	$\lvert\overline{V}\rvert/u_o$	$\overline{u}_r/u_o$	$\overline{v}_\theta/u_o$	$\overline{u}_r^2/u_o^2$	$\overline{v}_\theta^2/u_o^2$	$\overline{u_r v_\theta}/u_o^2$
8.000	0.053	0.3	26.5	26.5	0.1	0.93	0.24	0.00
7.333	0.053	0.0	29.5	29.5	0.0	1.11	0.28	0.00
6.666	0.053	0.1	32.8	32.8	0.0	1.29	0.36	0.00
6.000	0.053	0.1	37.2	37.2	0.0	1.47	0.46	-0.00
5.333	0.053	-0.3	41.7	41.7	-0.2	1.65	0.55	0.01
4.666	0.053	-0.0	47.8	47.8	-0.0	1.73	0.67	0.00
4.000	0.053	-0.0	54.6	54.6	-0.0	1.73	0.67	-0.00
3.333	0.053	0.2	61.2	61.2	0.2	1.68	0.64	-0.00
2.666	0.053	-0.0	67.8	67.8	-0.0	1.73	0.45	-0.00
2.000	0.053	-0.1	73.3	73.3	-0.1	1.83	0.36	-0.00
1.333	0.053	-0.3	75.9	75.9	-0.5	2.06	0.40	-0.01
0.666	0.053	-0.6	71.6	71.6	-0.8	2.36	0.76	0.00
0.000	0.053	-1.3	51.7	51.7	-1.2	2.71	1.30	-0.00

Note: β is in degrees; columns 4 - 9 are expressed as percentages

RADIAL TRAVERSE JET AT 15 DEGREES

r/d	z/d	β	$\lvert\bar{V}\rvert/u_o$	$\bar{u}_r/u_o$	$\bar{v}_\theta/u_o$	$\bar{u}_r^2/u_o^2$	$\bar{v}_\theta^2/u_o^2$	$\overline{u_r v_\theta}/u_o^2$
8.000	0.053	-0.1	26.2	26.2	-0.0	0.92	0.26	-0.01
7.333	0.053	-0.3	29.0	29.0	-0.1	1.10	0.27	-0.01
6.666	0.053	-0.0	32.3	32.3	-0.0	1.29	0.37	-0.02
6.000	0.053	1.0	36.6	36.6	0.6	1.49	0.46	-0.03
5.333	0.053	1.3	41.4	41.4	0.9	1.66	0.58	-0.04
4.666	0.053	1.7	46.9	46.9	1.4	1.78	0.65	-0.05
4.000	0.053	2.2	53.9	53.8	2.1	1.80	0.72	-0.04
3.333	0.053	2.7	60.8	60.8	2.9	1.81	0.61	-0.02
2.666	0.053	3.1	67.7	67.6	3.7	1.83	0.48	0.01
2.000	0.053	4.1	73.5	73.3	5.3	1.95	0.38	0.07
1.333	0.053	5.4	76.8	76.4	7.3	2.19	0.45	0.16
0.666	0.053	8.6	72.3	71.4	10.8	2.46	0.88	0.28
0.000	0.053	16.1	52.4	50.3	14.5	2.65	1.53	0.39

Note: β is in degrees; columns 4 - 9 are expressed as percentages

RADIAL TRAVERSE JET AT 45 DEGREES

r/d	z/d	β	$\lvert\bar{V}\rvert/u_o$	$\bar{u}_r/u_o$	$\bar{v}_\theta/u_o$	$\bar{u}_r^2/u_o^2$	$\bar{v}_\theta^2/u_o^2$	$\overline{u_r v_\theta}/u_o^2$
8.000	0.053	0.6	16.8	16.8	0.1	0.37	0.14	-0.01
7.333	0.053	1.0	18.6	18.6	0.3	0.47	0.15	-0.01
6.666	0.053	1.3	20.5	20.5	0.4	0.57	0.19	-0.01
6.000	0.053	2.5	23.3	23.3	1.0	0.73	0.23	-0.01
5.333	0.053	3.5	26.8	26.7	1.6	0.94	0.28	-0.01
4.666	0.053	4.7	31.2	31.1	2.5	1.19	0.34	-0.00
4.000	0.053	6.5	37.0	36.8	4.2	1.43	0.44	0.00
3.333	0.053	8.5	44.5	44.0	6.6	1.57	0.54	0.00
2.666	0.053	10.5	52.6	51.7	9.6	1.65	0.54	0.06
2.000	0.053	13.0	60.8	59.2	13.7	1.79	0.55	0.18
1.333	0.053	17.1	67.0	64.0	19.8	2.09	0.68	0.43
0.666	0.053	25.9	65.5	58.9	28.6	2.17	1.26	0.71
0.000	0.053	48.6	50.6	33.4	38.0	1.83	2.14	0.66

Note: β is in degrees; columns 4 - 9 are expressed as percentages

RADIAL TRAVERSE JET AT 90 DEGREES

r/d	z/d	β	$\lvert\overline{V}\rvert/u_o$	$\overline{u}_r/u_o$	$\overline{v}_\theta/u_o$	$\overline{u}_r^2/u_o^2$	$\overline{v}_\theta^2/u_o^2$	$\overline{u_r v_\theta}/u_o^2$
8.000	0.053	5.2	8.5	8.4	0.7	0.08	0.01	0.00
7.333	0.053	5.3	9.4	9.3	0.8	0.10	0.03	0.00
6.667	0.053	6.8	10.7	10.6	1.2	0.14	0.04	0.00
6.000	0.053	6.7	12.3	12.2	1.4	0.18	0.06	0.00
5.334	0.053	7.7	14.4	14.2	1.9	0.25	0.09	0.01
4.667	0.053	10.2	16.8	16.6	2.9	0.36	0.12	0.02
4.001	0.053	11.1	20.5	20.2	3.9	0.54	0.17	0.05
3.334	0.053	15.4	26.5	25.6	7.0	0.81	0.24	0.13
2.667	0.053	21.2	34.8	32.5	12.6	1.09	0.41	0.25
2.001	0.053	28.3	45.1	39.7	21.4	1.27	0.67	0.35
1.334	0.053	37.1	54.0	43.0	32.5	1.47	1.15	0.57
0.667	0.053	55.0	56.3	32.3	46.2	1.32	2.03	0.62

Note: β is in degrees; columns 4 - 9 are expressed as percentages

VERTICAL TRAVERSE JET AT 0 DEGREES

r/d	z/d	β	$\|\overline{V}\|/u_o$	$\overline{u}_r/u_o$	$\overline{v}_\theta/u_o$	$\overline{u}_r^2/u_o^2$	$\overline{v}_\theta^2/u_o^2$	$\overline{u_r v_\theta}/u_o^2$
3.000	0.053	0.0	58.2	58.2	-	1.53	-	-
3.000	0.066	0.0	66.0	66.0	-	1.45	-	-
3.000	0.080	0.0	62.0	62.0	-	1.37	-	-
3.000	0.093	0.0	62.2	62.2	-	1.29	-	-
3.000	0.106	0.0	61.9	61.9	-	1.24	-	-
3.000	0.120	0.0	61.3	61.3	-	1.17	-	-
3.000	0.133	0.0	60.2	60.2	-	1.13	-	-
3.000	0.146	0.0	59.0	59.0	-	1.12	-	-
3.000	0.160	0.0	57.6	57.6	-	1.13	-	-
3.000	0.173	0.0	55.9	55.9	-	1.12	-	-
3.000	0.213	0.0	51.3	51.3	-	1.21	-	-
3.000	0.266	0.0	44.7	44.7	-	1.27	-	-
3.000	0.319	0.0	38.5	38.5	-	1.30	-	-
3.000	0.373	0.0	32.7	32.7	-	1.24	-	-
3.000	0.426	0.0	27.4	27.4	-	1.15	-	-
3.000	0.480	0.0	23.0	23.0	-	1.04	-	-
3.000	0.533	0.0	19.2	19.2	-	0.87	-	-
3.000	0.586	0.0	15.9	15.9	-	0.74	-	-
3.000	0.640	0.0	13.4	13.4	-	0.59	-	-
3.000	0.693	0.0	11.0	11.0	-	0.43	-	-
3.000	0.746	0.0	9.1	9.1	-	0.31	-	-
3.000	0.800	0.0	7.8	7.8	-	0.23	-	-
3.000	0.853	0.0	6.9	6.9	-	0.17	-	-
3.000	0.906	0.0	6.1	6.1	-	0.11	-	-
3.000	0.960	0.0	5.5	5.5	-	0.08	-	-
3.000	1.013	0.0	5.0	5.0	-	0.05	-	-
3.000	1.066	0.0	4.8	4.8	-	0.04	-	-

Note: β is in degrees; columns 4 - 9 are expressed as percentages

RADIAL TRAVERSE JET AT 135 DEGREES

r/d	z/d	β	$\lvert\overline{V}\rvert/u_o$	$\overline{u}_r/u_o$	$\overline{v}_\theta/u_o$	$\overline{u}_r^2/u_o^2$	$\overline{v}_\theta^2/u_o^2$	$\overline{u_r v_\theta}/u_o^2$
7.999	0.053	1.7	3.9	3.9	0.1	0.00	-0.00	0.00
7.333	0.053	3.9	4.3	4.3	0.2	0.01	-0.00	0.00
6.666	0.053	4.2	5.3	5.3	0.3	0.02	-0.00	0.00
5.999	0.053	5.5	6.3	6.3	0.6	0.04	0.00	0.00
5.333	0.053	8.3	7.7	7.6	1.1	0.07	0.01	0.00
4.666	0.053	8.6	9.6	9.5	1.4	0.12	0.03	0.01
3.999	0.053	12.0	12.5	12.3	2.6	0.22	0.06	0.02
3.333	0.053	16.3	16.8	16.1	4.7	0.38	0.13	0.07
2.666	0.053	26.6	24.2	21.7	10.8	0.66	0.31	0.23
1.999	0.053	37.5	35.1	27.8	21.4	0.98	0.86	0.40
1.333	0.053	54.4	41.4	24.0	33.6	1.12	1.85	0.53
0.666	0.053	82.4	42.3	5.5	42.0	0.17	2.42	0.29

Note: β is in degrees; columns 4 - 9 are expressed as percentages

RADIAL TRAVERSE JET AT 180 DEGREES

r/d	z/d	β	$\|\overline{V}\|/u_o$	$\overline{u}_r/u_o$	$\overline{v}_\theta/u_o$	$\overline{u}_r^2/u_o^2$	$\overline{v}_\theta^2/u_o^2$	$\overline{u_r v_\theta}/u_o^2$
8.000	0.053	-0.8	3.2	3.2	-0.0	-0.00	-0.01	-0.00
7.333	0.053	-3.8	3.7	3.7	-0.2	0.00	-0.01	0.00
6.666	0.053	0.4	4.0	4.0	0.0	0.01	-0.00	-0.00
6.000	0.053	0.7	4.6	4.6	0.0	0.02	-0.00	-0.00
5.333	0.053	-0.8	5.8	5.8	-0.0	0.04	-0.00	-0.00
4.666	0.053	-0.3	7.5	7.5	-0.0	0.08	0.00	-0.00
4.000	0.053	1.1	9.8	9.8	0.1	0.15	0.03	-0.00
3.333	0.053	0.2	13.7	13.7	0.0	0.30	0.08	0.00
2.666	0.053	1.5	20.2	20.2	0.5	0.68	0.24	0.01
2.000	0.053	3.3	24.4	24.3	1.4	1.19	0.56	0.04
1.333	0.053	7.3	17.9	17.8	2.3	0.73	0.71	0.04
0.666	0.053	-2.6	27.4	27.4	-1.2	1.92	0.81	-0.11

Note: β is in degrees; columns 4 - 9 are expressed as percentages

RADIAL TRAVERSE JET AT 30 DEGREES

r/d	z/d	β	$\lvert\bar{V}\rvert/u_o$	$\bar{u}_r/u_o$	$\bar{v}_\theta/u_o$	$\bar{u}_r^2/u_o^2$	$\bar{v}_\theta^2/u_o^2$	$\overline{u_r v_\theta}/u_o^2$
8.000	0.053	-0.5	20.2	20.2	-0.2	0.28	-0.07	-0.00
7.333	0.053	-0.7	21.9	21.9	-0.2	0.40	-0.09	-0.00
6.666	0.053	-0.6	24.0	24.0	-0.2	0.54	-0.10	-0.00
6.000	0.053	0.9	27.5	27.5	0.4	0.76	-0.10	0.00
5.333	0.053	1.5	31.0	31.0	0.8	0.96	-0.03	0.01
4.666	0.053	3.3	35.6	35.6	2.0	1.14	0.09	0.01
4.000	0.053	4.2	41.2	41.1	3.0	1.25	0.30	-0.00
3.333	0.053	5.3	47.8	47.6	4.4	1.24	0.44	0.00
2.666	0.053	6.8	54.1	53.7	6.4	1.20	0.46	0.01
2.000	0.053	8.5	59.9	59.2	8.9	1.22	0.44	0.07
1.333	0.053	11.4	63.8	62.5	12.6	1.34	0.49	0.17
0.666	0.053	17.4	61.6	58.8	18.4	1.49	0.78	0.30
0.000	0.053	32.2	47.2	39.9	25.1	1.55	1.13	0.54

Note: β is in degrees; columns 4 - 9 are expressed as percentages

RADIAL TRAVERSE JET AT 60 DEGREES

r/d	z/d	β	$\lvert\overline{V}\rvert/u_o$	$\overline{u}_r/u_o$	$\overline{v}_\theta/u_o$	$\overline{u}_r^2/u_o^2$	$\overline{v}_\theta^2/u_o^2$	$\overline{u_r v_\theta}/u_o^2$
8.000	0.053	2.3	20.9	20.9	0.8	0.19	0.36	-0.02
7.333	0.053	3.7	21.4	21.4	1.3	0.17	0.35	-0.01
6.666	0.053	3.7	22.1	22.0	1.4	0.18	0.31	-0.01
6.000	0.053	5.5	23.3	23.2	2.2	0.20	0.27	-0.01
5.333	0.053	5.1	25.0	24.9	2.2	0.28	0.18	-0.00
4.666	0.053	5.8	27.7	27.6	2.8	0.45	0.03	0.02
4.000	0.053	7.5	31.7	31.4	4.1	0.71	-0.07	0.08
3.333	0.053	9.8	37.4	36.8	6.4	0.97	-0.06	0.16
2.666	0.053	13.7	44.8	43.5	10.6	1.12	0.14	0.21
2.000	0.053	17.7	52.3	49.8	15.9	1.21	0.38	0.25
1.333	0.053	23.4	58.4	53.6	23.2	1.32	0.59	0.37
0.666	0.053	34.8	59.5	48.9	34.0	1.29	0.98	0.62
0.000	0.053	63.5	50.8	22.6	45.5	0.68	1.60	0.62

Note: β is in degrees; columns 4 - 9 are expressed as percentages

VERTICAL TRAVERSE JET AT 90 DEGREES

r/d	z/d	β	$\lvert\bar{V}\rvert/u_o$	$\bar{u}_r/u_o$	$\bar{v}_\theta/u_o$	$\bar{u}_r^2/u_o^2$	$\bar{v}_\theta^2/u_o^2$	$\overline{u_r v_\theta}/u_o^2$
1.333	0.013	35.6	49.5	40.2	28.8	1.89	1.38	0.68
1.333	0.026	36.0	53.3	43.1	31.4	1.81	1.33	0.69
1.333	0.040	36.8	54.1	43.3	32.4	1.64	1.25	0.63
1.333	0.053	37.4	54.2	43.0	32.9	1.48	1.15	0.57
1.333	0.066	38.3	53.7	42.1	33.3	1.33	1.10	0.50
1.333	0.079	39.2	52.9	41.0	33.5	1.23	1.04	0.44
1.333	0.093	39.3	52.0	40.2	33.0	1.13	1.00	0.39
1.333	0.106	40.3	50.9	38.8	33.0	1.06	0.96	0.34
1.333	0.119	41.5	49.8	37.2	33.0	1.01	0.94	0.32
1.333	0.133	43.0	48.5	35.4	33.1	0.96	0.92	0.28
1.333	0.186	45.8	43.1	30.0	30.9	0.86	0.85	0.27
1.333	0.239	48.1	38.6	25.7	28.7	0.79	0.84	0.30
1.333	0.293	50.7	34.0	21.5	26.3	0.71	0.81	0.33
1.333	0.346	54.1	30.4	17.8	24.7	0.61	0.80	0.34
1.333	0.399	56.5	27.0	14.9	22.6	0.53	0.77	0.31
1.333	0.453	59.9	24.4	12.2	21.1	0.44	0.75	0.30
1.333	0.519	63.3	20.8	9.3	18.6	0.38	0.70	0.26
1.333	0.586	68.8	18.2	6.5	16.9	0.31	0.65	0.21

Note: β is in degrees; columns 4 - 9 are expressed as percentages

VERTICAL TRAVERSE JET AT 90 DEGREES

r/d	z/d	β	$\|\overline{V}\|/u_o$	$\overline{u}_r/u_o$	$\overline{v}_\theta/u_o$	$\overline{u}_r^2/u_o^2$	$\overline{v}_\theta^2/u_o^2$	$\overline{u_r v_\theta}/u_o^2$
3.000	0.013	27.1	23.6	21.0	10.8	0.76	0.30	0.22
3.000	0.026	26.7	27.3	24.4	12.3	0.88	0.37	0.27
3.000	0.040	28.8	29.3	25.7	14.1	0.88	0.39	0.29
3.000	0.053	30.7	30.1	25.9	15.4	0.85	0.42	0.31
3.000	0.066	32.7	30.3	25.5	16.4	0.80	0.44	0.33
3.000	0.080	34.4	30.3	25.0	17.1	0.75	0.46	0.35
3.000	0.093	36.7	30.4	24.4	18.2	0.71	0.51	0.35
3.000	0.106	38.7	30.1	23.4	18.8	0.68	0.54	0.35
3.000	0.120	40.8	29.7	22.4	19.4	0.64	0.58	0.35
3.000	0.133	42.3	29.3	21.6	19.7	0.61	0.61	0.35
2.999	0.203	46.2	25.5	17.6	18.4	0.53	0.66	0.33
2.999	0.269	50.1	21.1	13.5	16.2	0.43	0.66	0.28
2.999	0.336	56.3	17.1	9.5	14.2	0.33	0.61	0.17
2.999	0.403	61.6	13.5	6.4	11.9	0.25	0.50	0.08

Note: β is in degrees; columns 4 - 9 are expressed as percentages

VERTICAL TRAVERSE JET AT 0 DEGREES

r/d	z/d	β	$\|\overline{V}\|/u_o$	$\overline{u}_r/u_o$	$\overline{v}_\theta/u_o$	$\overline{u}_r^2/u_o^2$	$\overline{v}_\theta^2/u_o^2$	$\overline{u_r v_\theta}/u_o^2$
1.333	0.013	0.0	64.6	64.6	0.0	2.36	0.77	0.01
1.333	0.026	0.0	68.0	68.0	0.0	2.48	0.65	0.00
1.333	0.040	0.0	71.4	71.4	0.0	2.39	0.53	0.01
1.333	0.053	0.0	72.2	72.2	0.0	2.17	0.42	0.01
1.333	0.080	0.0	72.0	72.0	0.0	1.87	0.41	0.01
1.333	0.106	0.0	70.7	70.7	0.0	1.49	0.39	0.01
1.333	0.133	0.0	68.8	68.8	0.0	1.24	0.41	0.01
1.333	0.160	0.0	66.3	66.3	0.0	1.12	0.46	0.01
1.333	0.186	0.0	63.7	63.7	0.0	1.07	0.50	0.01
1.333	0.213	0.0	60.9	60.9	0.0	1.05	0.55	0.00
1.333	0.240	0.0	58.1	58.1	0.0	1.07	0.58	0.00
1.333	0.266	0.0	55.2	55.2	0.0	1.09	0.61	0.01
1.333	0.293	0.0	52.7	52.7	0.0	1.10	0.66	0.01
1.333	0.319	0.0	50.0	50.0	0.0	1.14	0.64	0.01
1.333	0.453	0.0	37.8	37.8	0.0	1.23	0.52	0.01
1.333	0.586	0.0	28.0	28.0	0.0	1.10	0.35	0.01
1.333	0.719	0.0	20.5	20.5	0.0	0.85	0.25	0.02
1.333	0.853	0.0	14.4	14.4	0.0	0.60	0.15	0.01
1.333	0.986	0.0	10.2	10.2	0.0	0.35	0.10	0.00
1.333	1.120	0.0	7.0	7.0	0.0	0.17	0.07	0.00
1.333	1.253	0.0	5.3	5.3	0.0	0.07	0.03	0.00
1.333	1.386	0.0	4.2	4.2	0.0	0.02	0.01	0.00

Note: β is in degrees; columns 4 - 9 are expressed as percentages

VERTICAL TRAVERSE JET AT 45 DEGREES

r/d	z/d	β	$\overline{\lvert V \rvert}/u_o$	$\overline{u}_r/u_o$	$\overline{v}_\theta/u_o$	$\overline{u}_r^2/u_o^2$	$\overline{v}_\theta^2/u_o^2$	$\overline{u_r v_\theta}/u_o^2$
1.333	0.013	17.0	68.8	65.8	20.1	2.59	0.77	0.53
1.333	0.026	17.5	70.4	67.1	21.2	2.41	0.65	0.53
1.333	0.040	17.7	70.7	67.3	21.5	2.14	0.62	0.49
1.333	0.053	17.7	70.3	67.0	21.4	1.90	0.61	0.42
1.333	0.066	18.2	69.4	65.9	21.7	1.73	0.59	0.38
1.333	0.079	18.7	68.2	64.6	21.9	1.57	0.60	0.34
1.333	0.093	18.3	67.1	63.6	21.4	1.46	0.61	0.31
1.333	0.106	19.1	65.5	61.9	21.4	1.36	0.62	0.27
1.333	0.119	19.6	64.1	60.4	21.5	1.29	0.65	0.23
1.333	0.133	20.4	62.7	58.8	21.9	1.24	0.67	0.24
1.333	0.186	19.8	57.6	54.5	18.6	1.13	0.69	0.15
1.333	0.239	20.1	51.5	48.4	17.7	1.13	0.69	0.15
1.333	0.293	22.0	46.6	43.2	17.4	1.13	0.68	0.16
1.333	0.346	22.1	41.1	38.0	15.5	1.14	0.62	0.21
1.333	0.399	24.3	37.1	33.8	15.3	1.10	0.56	0.24
1.333	0.453	25.6	32.8	29.6	14.2	1.03	0.48	0.29
1.333	0.506	24.5	29.6	26.9	12.3	1.05	0.33	0.39
1.333	0.559	26.8	26.0	23.2	11.8	0.87	0.37	0.30
1.333	0.613	23.3	22.7	20.8	9.0	0.78	0.31	0.26
1.333	0.666	27.2	19.7	17.5	9.0	0.68	0.30	0.24
1.333	0.719	28.0	17.7	15.6	8.3	0.60	0.26	0.24
1.333	0.773	27.0	15.2	13.5	6.9	0.53	0.23	0.18
1.333	0.826	25.3	13.7	12.4	5.9	0.46	0.18	0.17
1.333	0.879	24.4	12.4	11.3	5.1	0.38	0.15	0.15
1.333	0.933	25.3	10.7	9.6	4.5	0.31	0.10	0.13
1.333	0.986	24.7	8.6	7.8	3.6	0.23	0.13	0.05
1.333	1.039	24.0	7.9	7.2	3.2	0.19	0.11	0.05

Note: β is in degrees; columns 4 - 9 are expressed as percentages

VERTICAL TRAVERSE JET AT 45 DEGREES

r/d	z/d	β	$\|\overline{V}\|/u_o$	$\overline{u}_r/u_o$	$\overline{v}_\theta/u_o$	$\overline{u}_r^2/u_o^2$	$\overline{v}_\theta^2/u_o^2$	$\overline{u_r v_\theta}/u_o^2$
3.000	0.013	8.9	50.2	49.6	7.7	1.94	0.69	0.00
3.000	0.026	9.5	52.8	52.0	8.7	1.82	0.63	0.05
3.000	0.039	8.9	53.4	52.7	8.3	1.77	0.62	0.05
3.000	0.053	8.7	53.8	53.2	8.2	1.68	0.64	0.05
3.000	0.066	8.8	53.6	52.9	8.2	1.61	0.68	0.06
3.000	0.079	8.4	52.9	52.3	7.7	1.59	0.64	0.09
3.000	0.093	8.6	52.1	51.5	7.8	1.54	0.66	0.10
3.000	0.106	8.9	51.0	50.4	7.9	1.52	0.69	0.12
3.000	0.119	8.9	50.1	49.5	7.7	1.51	0.69	0.13
3.000	0.133	9.0	49.0	48.4	7.6	1.51	0.73	0.13
3.000	0.186	9.4	43.3	42.8	7.1	1.56	0.73	0.18
3.000	0.240	10.3	37.7	37.1	6.7	1.52	0.69	0.21
3.000	0.293	12.1	32.0	31.3	6.7	1.40	0.65	0.23
3.000	0.346	14.0	26.7	25.9	6.4	1.25	0.55	0.25
3.000	0.400	14.2	22.3	21.6	5.4	1.01	0.51	0.23
3.000	0.453	15.8	18.5	17.8	5.0	0.79	0.44	0.21
3.000	0.506	15.1	15.3	14.8	4.0	0.60	0.37	0.16
3.000	0.560	16.5	12.8	12.2	3.6	0.42	0.31	0.11
3.000	0.613	15.3	10.8	10.4	2.8	0.32	0.25	0.07
3.000	0.666	14.9	9.2	8.9	2.3	0.23	0.18	0.04
3.000	0.720	14.4	8.0	7.7	1.8	0.16	0.14	0.02
3.000	0.773	14.9	7.1	6.9	1.8	0.11	0.10	0.00
3.000	0.826	12.1	6.4	6.3	1.3	0.07	0.07	0.00
3.000	0.879	12.1	5.8	5.6	1.4	0.05	0.05	0.00
3.000	0.933	11.0	5.4	5.3	1.0	0.03	0.03	0.00
3.000	0.986	10.3	5.2	5.1	0.9	0.02	0.02	0.00
3.000	1.040	5.5	4.9	4.8	0.4	0.01	0.01	0.00

Note: β is in degrees; columns 4 - 9 are expressed as percentages

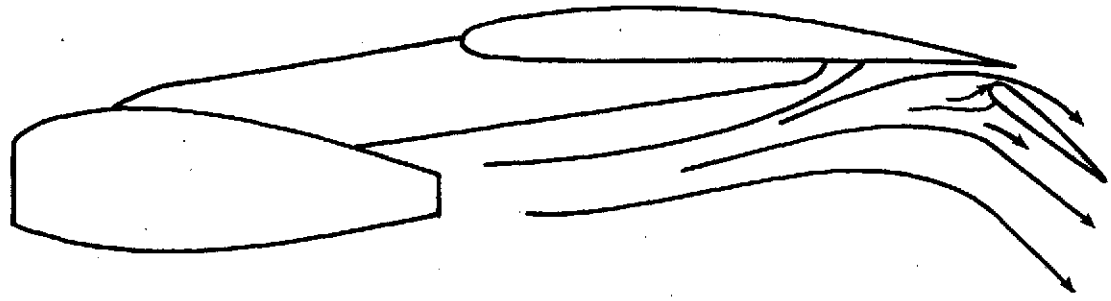

Figure 1. The externally blown flap configuration for STOL aircraft.

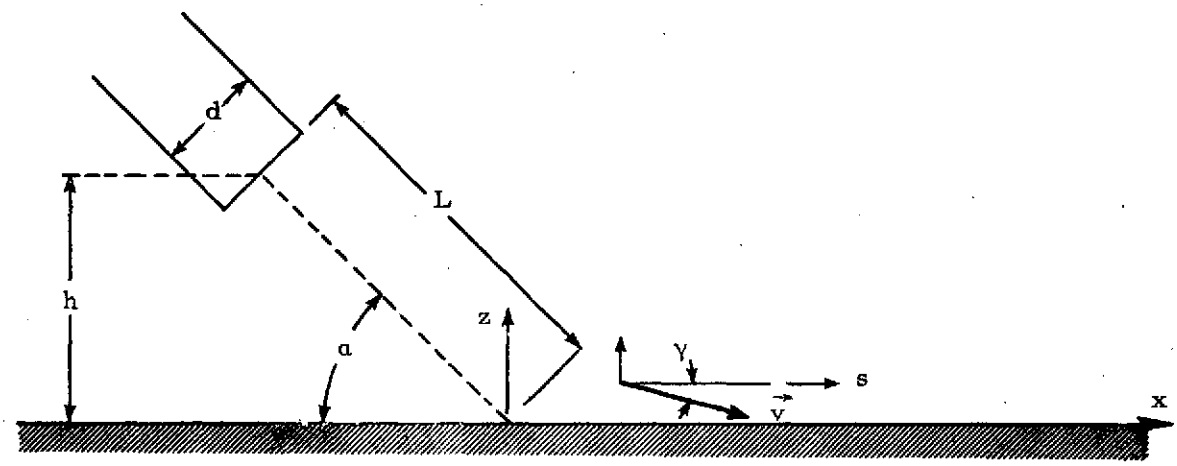

a. Side View

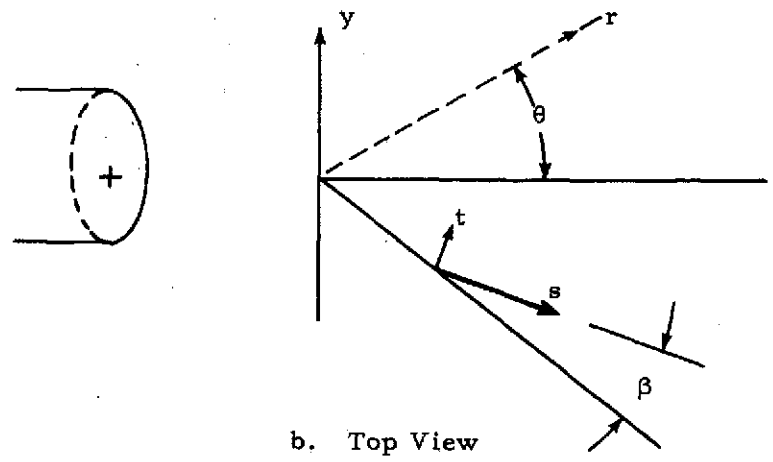

b. Top View

Figure 2. Nomenclature for the oblique jet impingement flow.

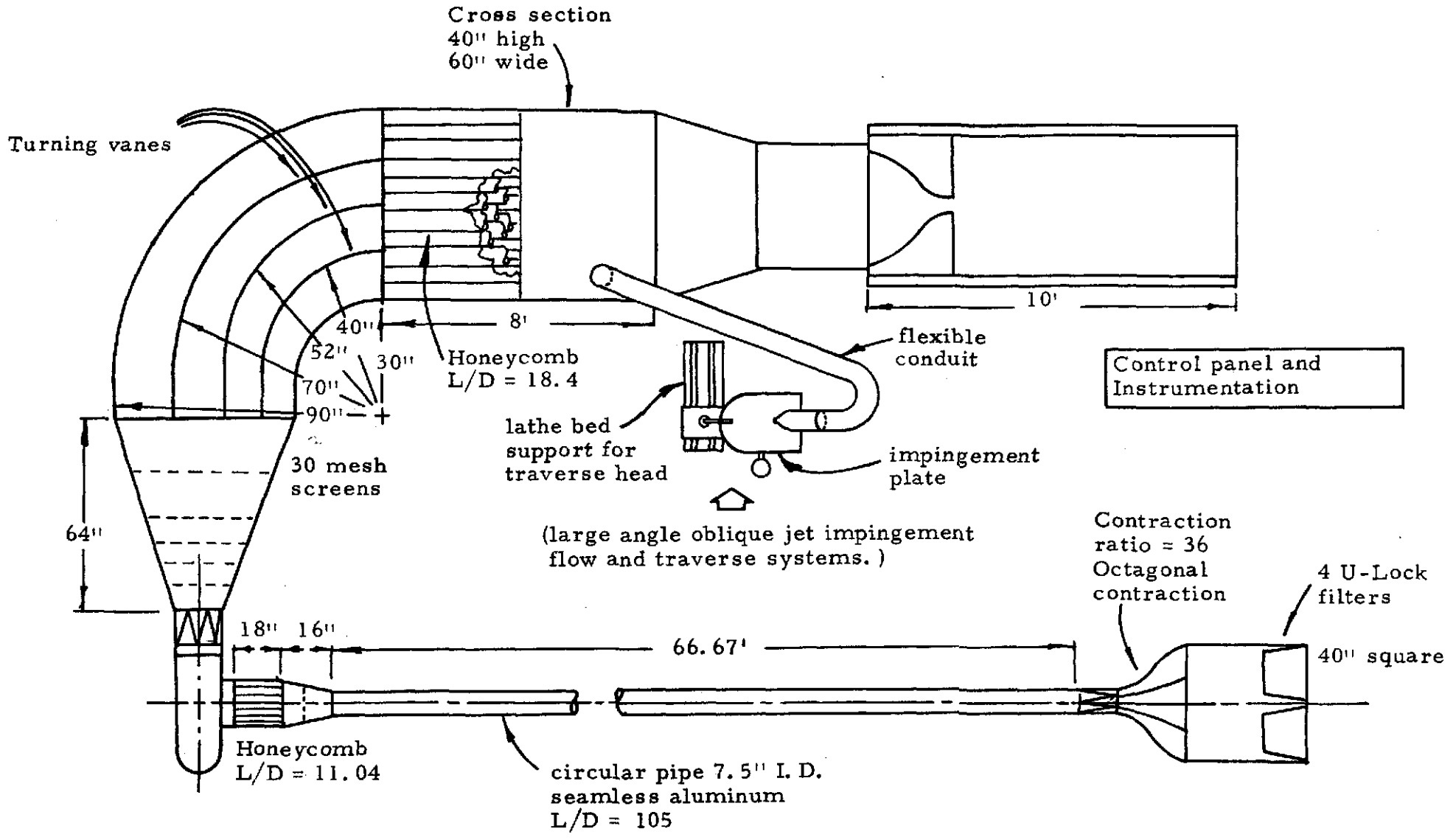

Figure 3. Schematic of laboratory.

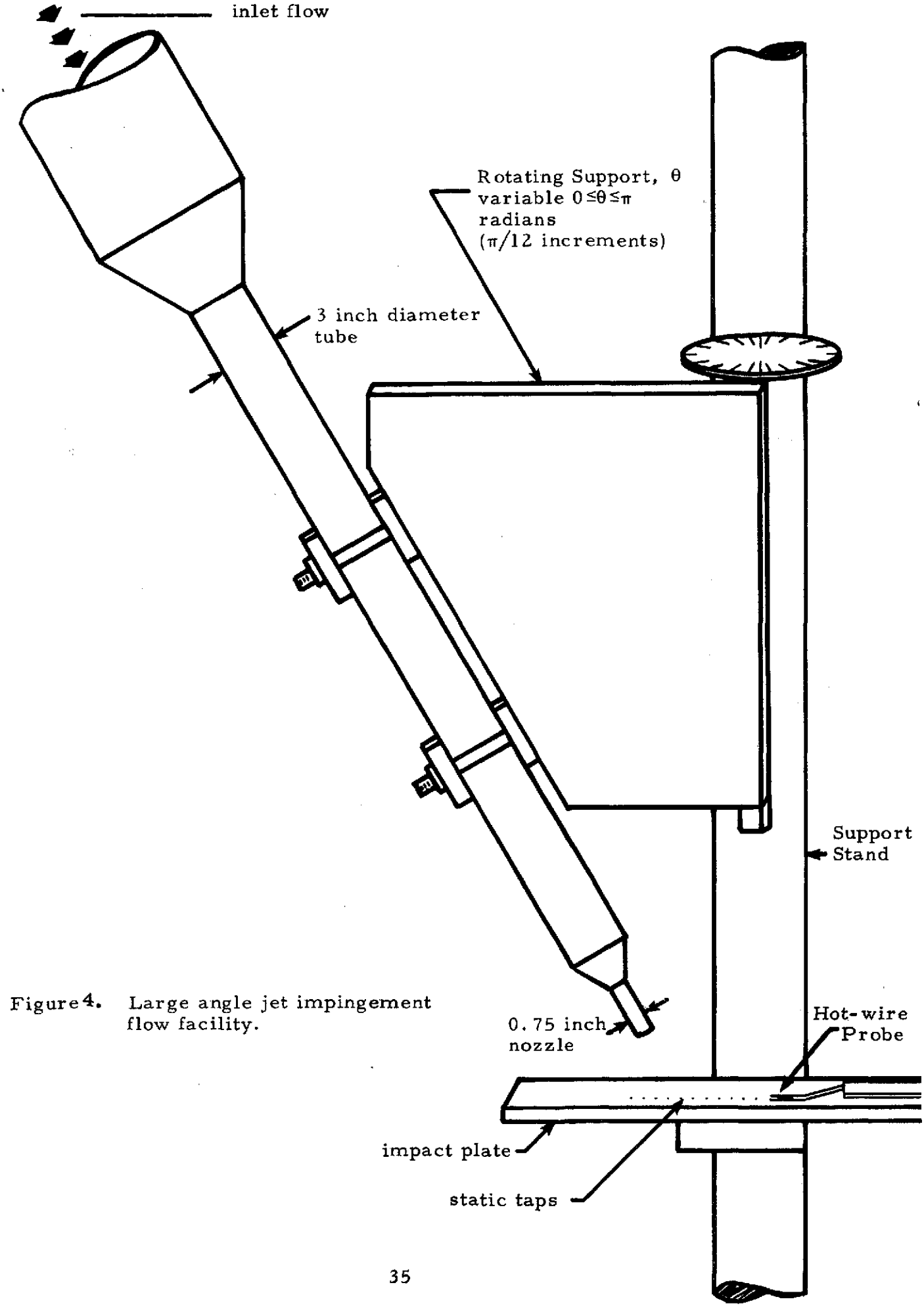

Figure 4. Large angle jet impingement flow facility.

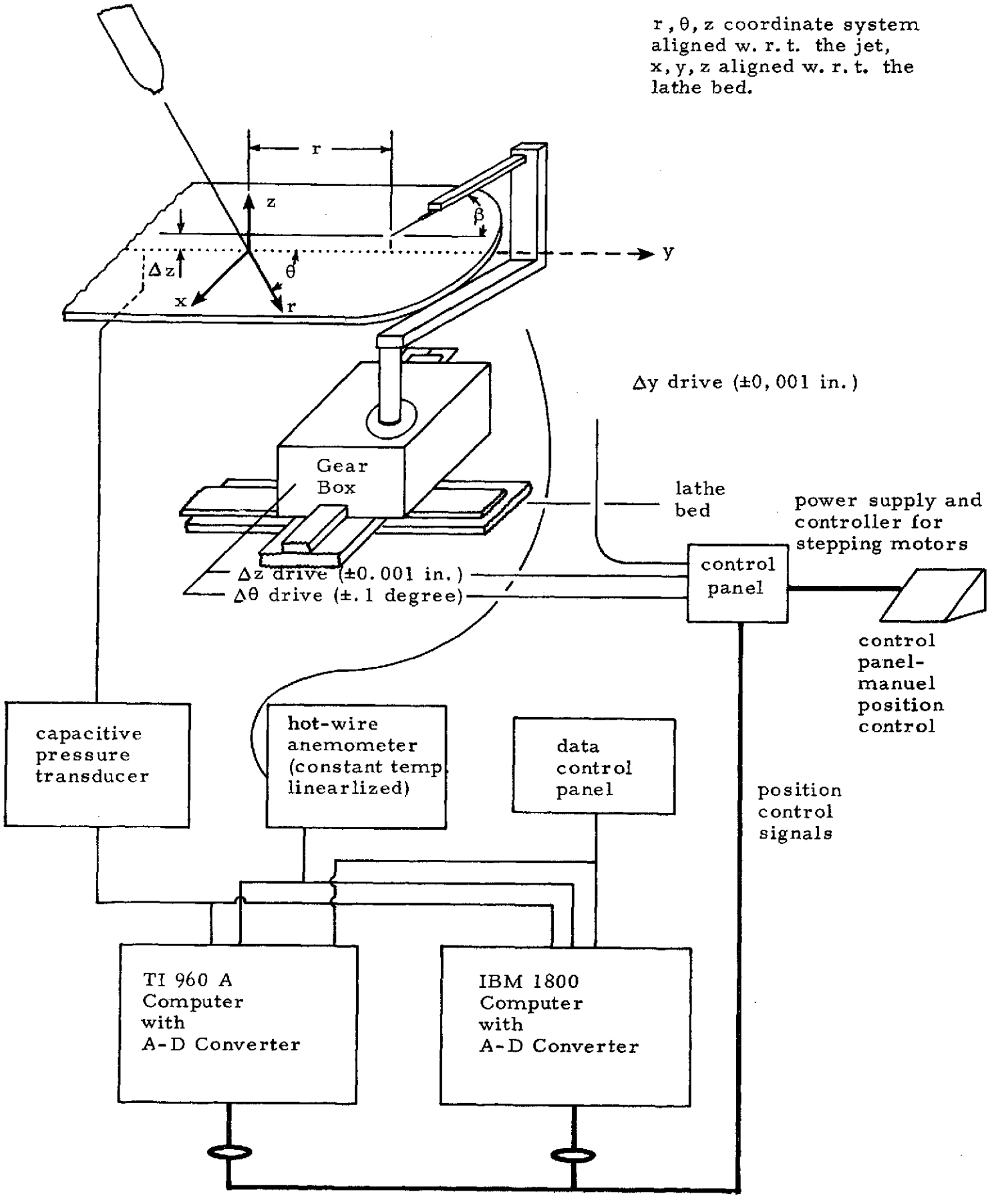

Figure 5. Schematic of data acquisition facility.

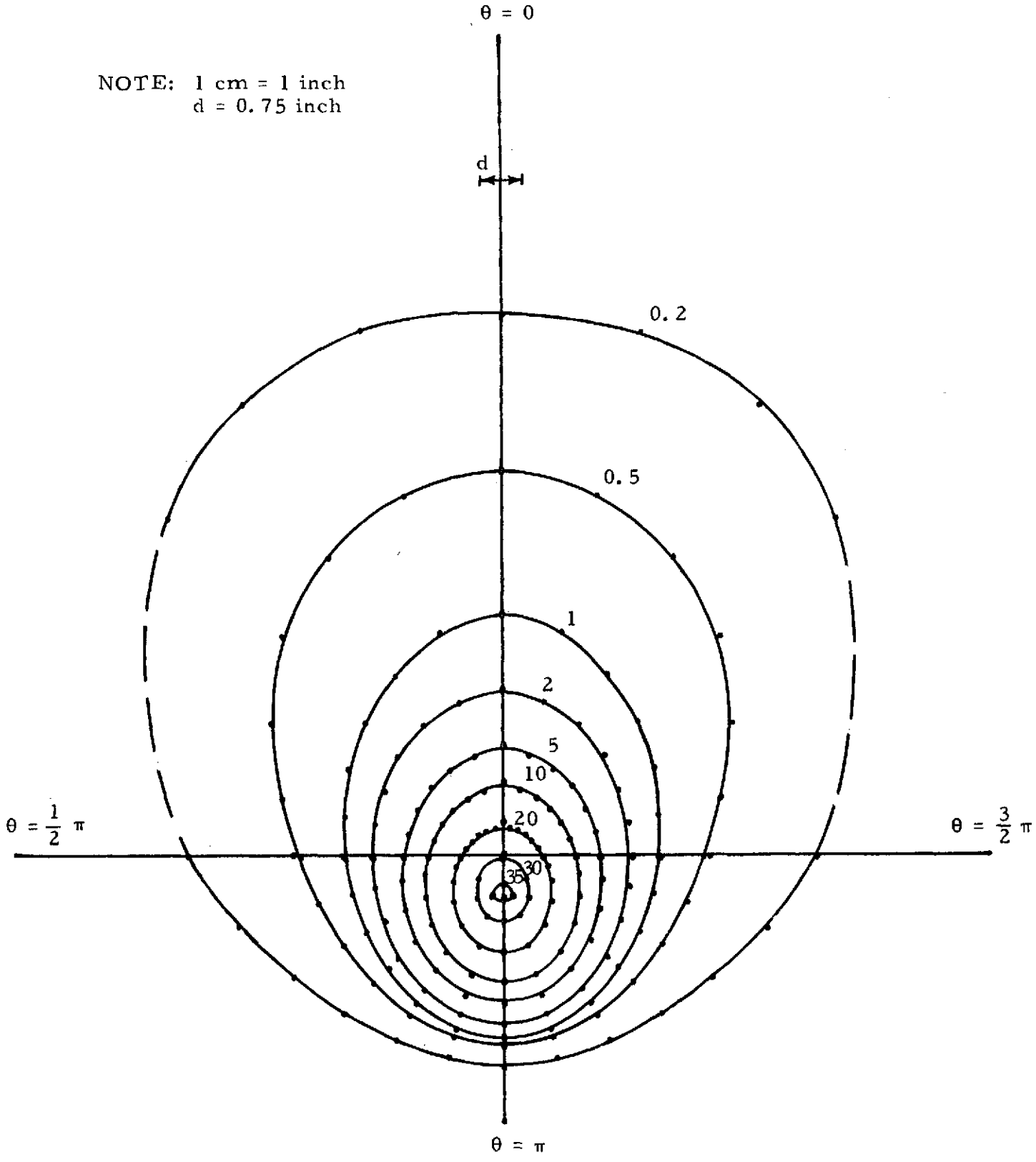

(a) Complete data set

Figure 6. Surface pressure isobar contours. α = 45 degrees, L/d = 7, jet Reynolds number = 4.8×10^4.

Contours represent level curves of $100 \dfrac{(p - p_{atm})}{\rho u_o^2 \lambda \sin \alpha}$

$\lambda = \int_{A_{jet}} \rho u^2 dA / \rho u_p^2 A_{jet}$, $\lambda = 0.809$ taken from [5].

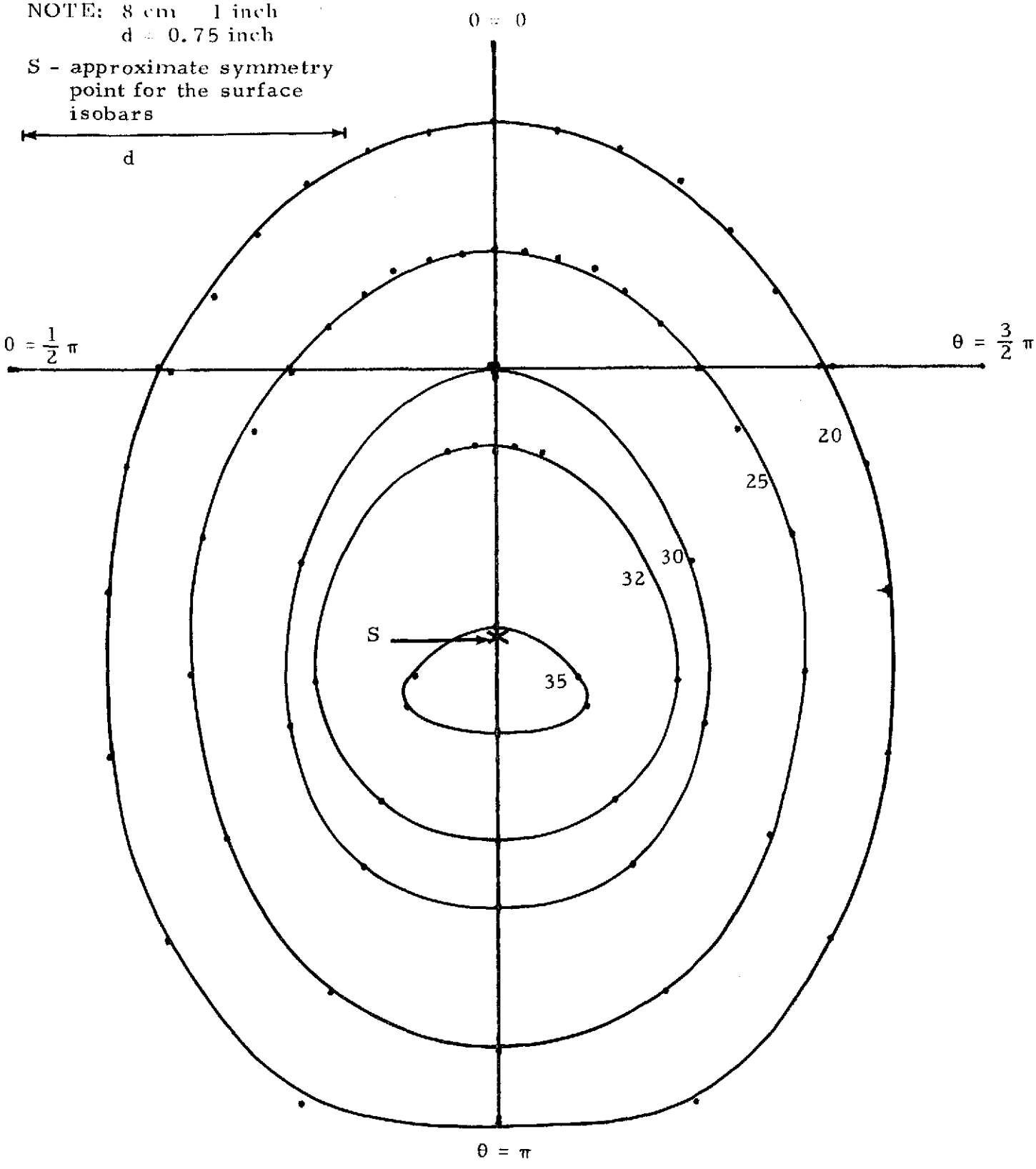

Figure 6b. Expanded scale to show detail of the maximum pressure region.

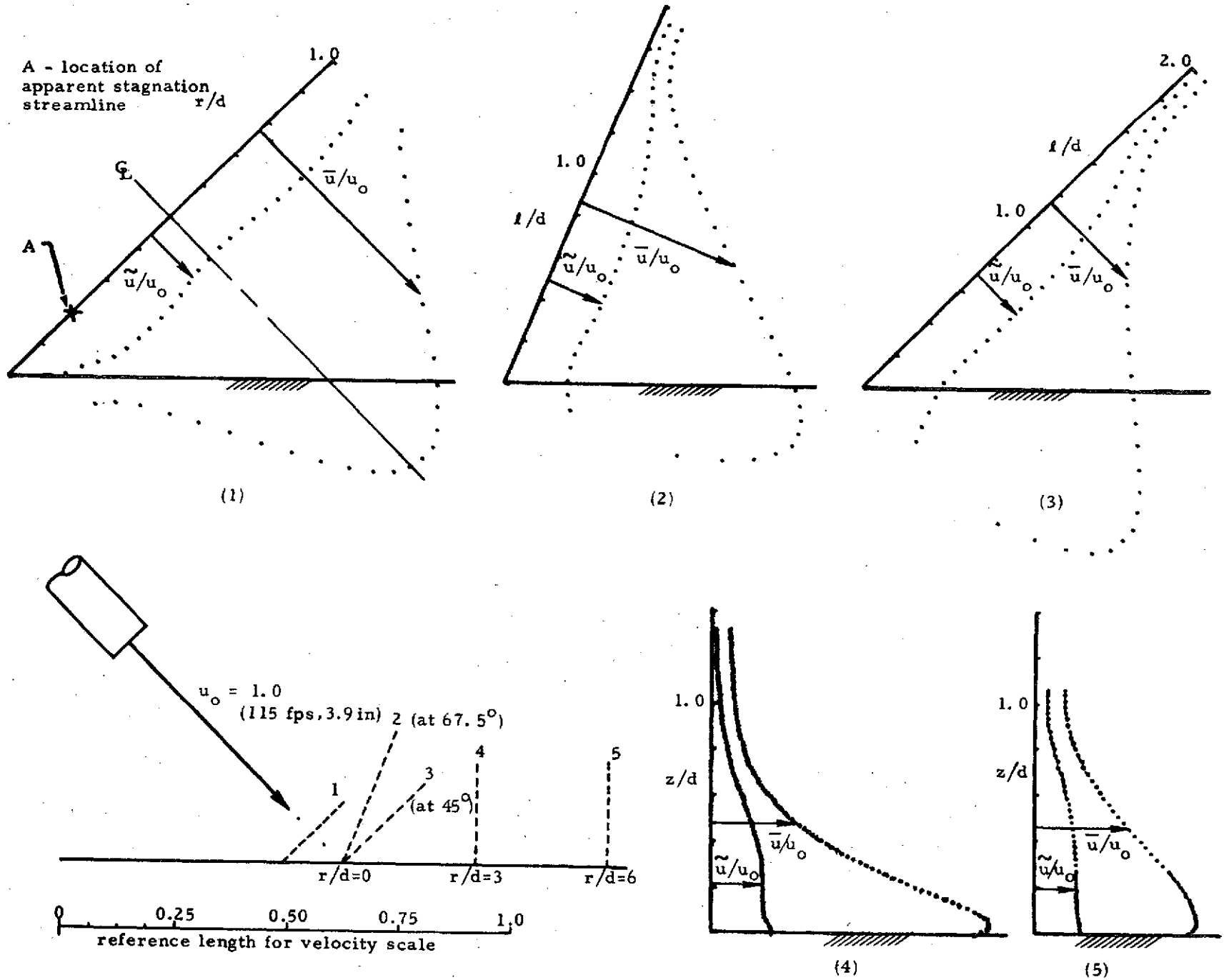

Figure 7. Velocity magnitude traverses in the $\theta = 0$, $\theta = \pi$ plane.

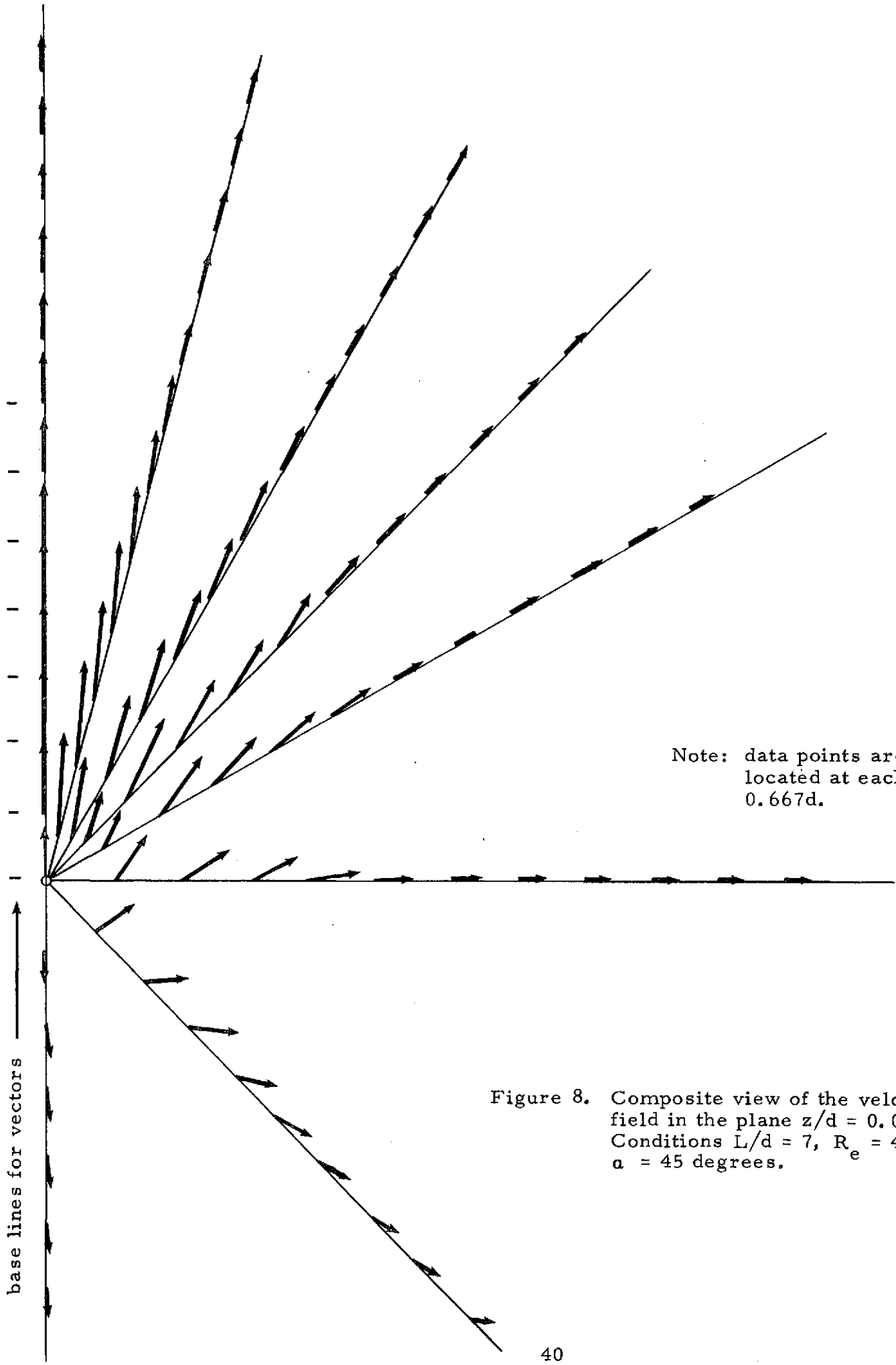

Note: data points are located at each 0.667d.

Figure 8. Composite view of the velocity field in the plane z/d = 0.053. Conditions L/d = 7, R_e = 4.8 x 10^4, α = 45 degrees.

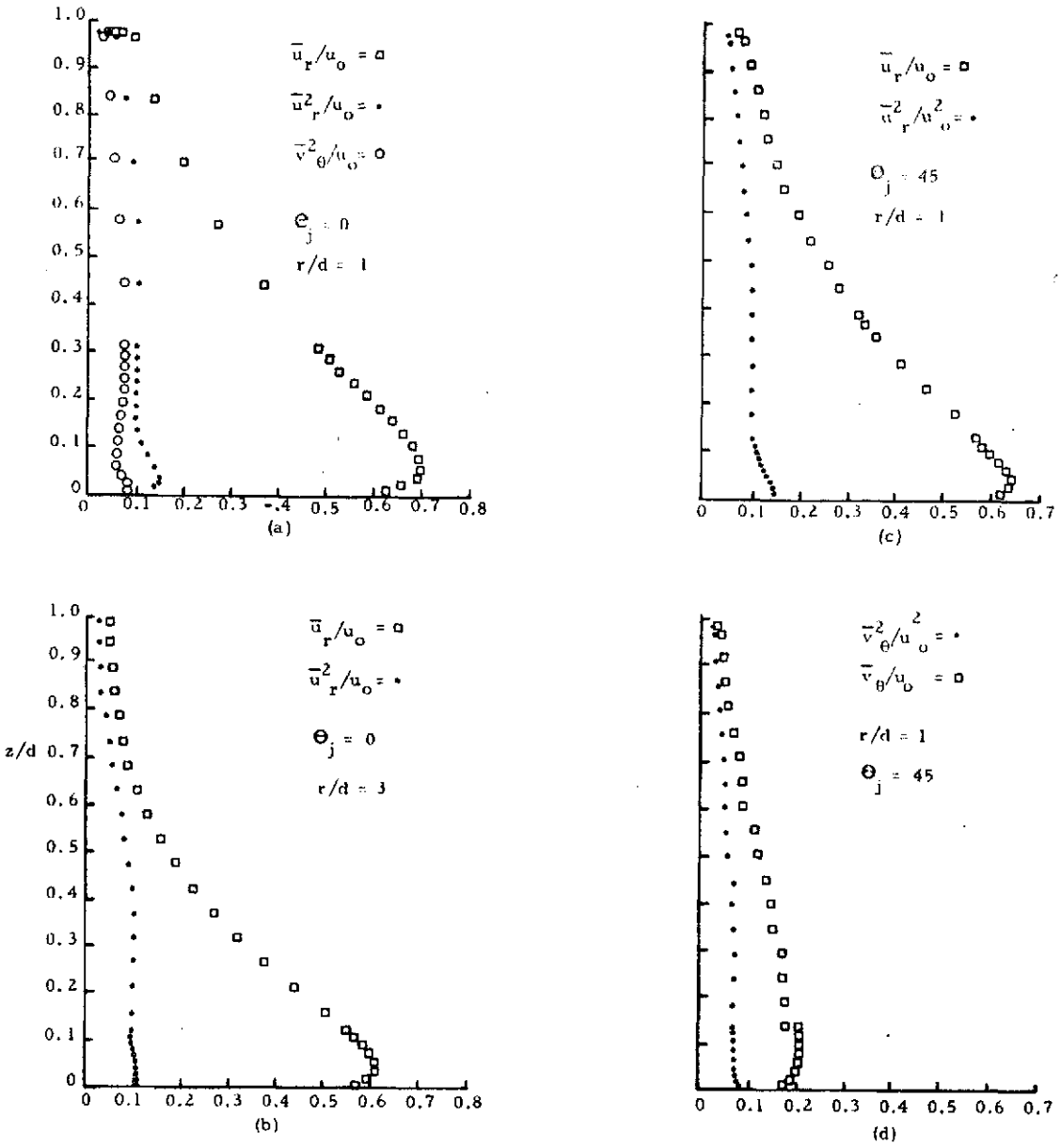

Figure 9. Vertical velocity traverses.

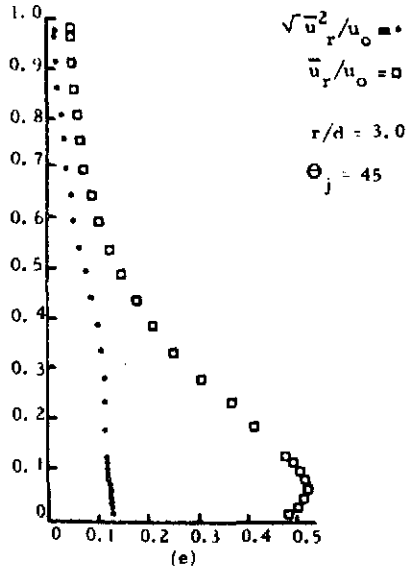
$\sqrt{\overline{u}^2_r}/u_o$ =•
$\overline{u}_r/u_o$ =□
r/d = 3.0
Θ_j = 45
(e)

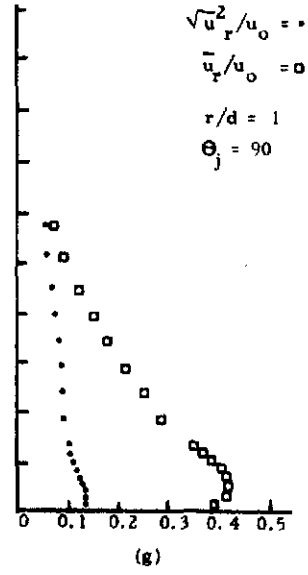
$\sqrt{\overline{u}^2_r}/u_o$ = •
$\overline{u}_r/u_o$ =□
r/d = 1
Θ_j = 90
(g)

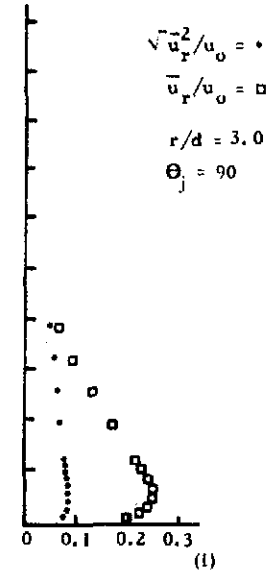
$\sqrt{\overline{u}^2_r}/u_o$ = •
$\overline{u}_r/u_o$ = □
r/d = 3.0
Θ_j = 90
(i)

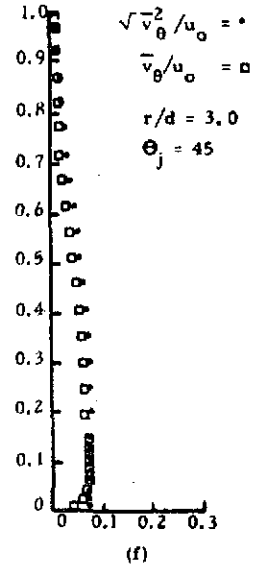
$\sqrt{\overline{v}^2_\theta}/u_o$ = •
$\overline{v}_\theta/u_o$ = □
r/d = 3.0
Θ_j = 45
(f)

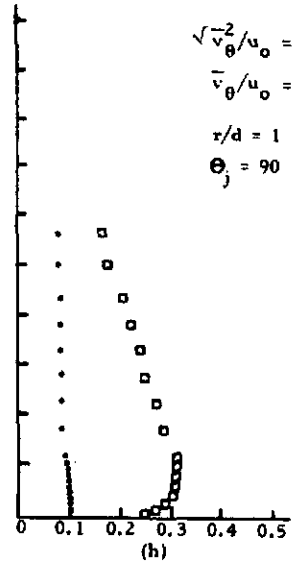
$\sqrt{\overline{v}^2_\theta}/u_o$ = •
$\overline{v}_\theta/u_o$ = □
r/d = 1
Θ_j = 90
(h)

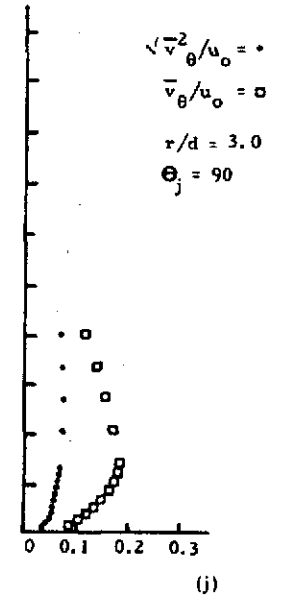
$\sqrt{\overline{v}^2_\theta}/u_o$ = •
$\overline{v}_\theta/u_o$ = □
r/d = 3.0
Θ_j = 90
(j)

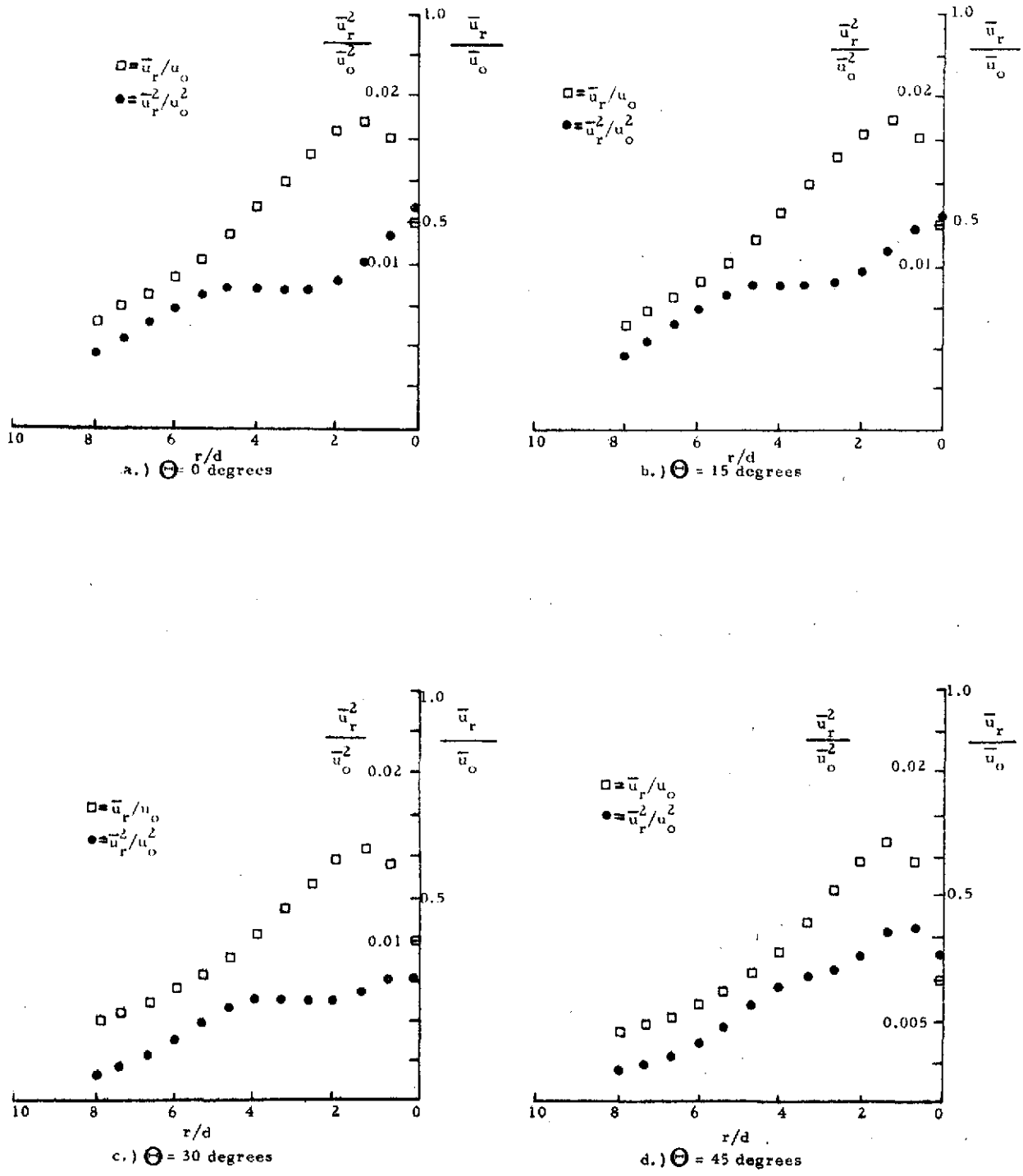

Figure 10. Radial traverses of the radial velocity and the normal Reynolds stress. (Presentation is to allow the magnitude of $\overline{u}_r^2 \, \partial\overline{u}_r/\partial r$.)

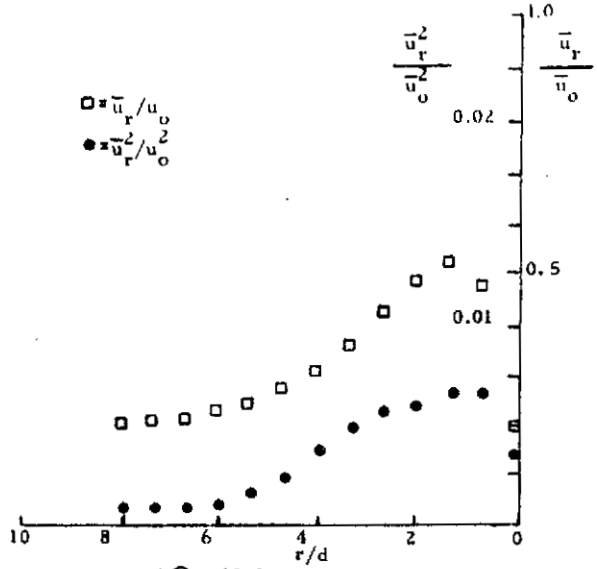

e.) Θ = 60 degrees

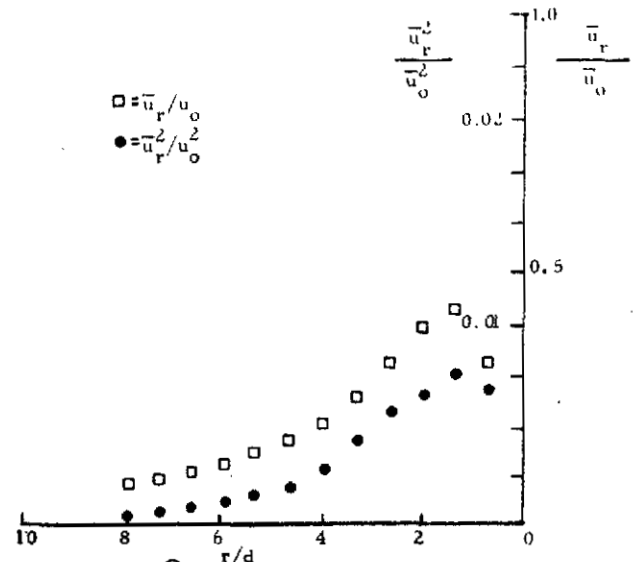

f.) Θ = 90 degrees

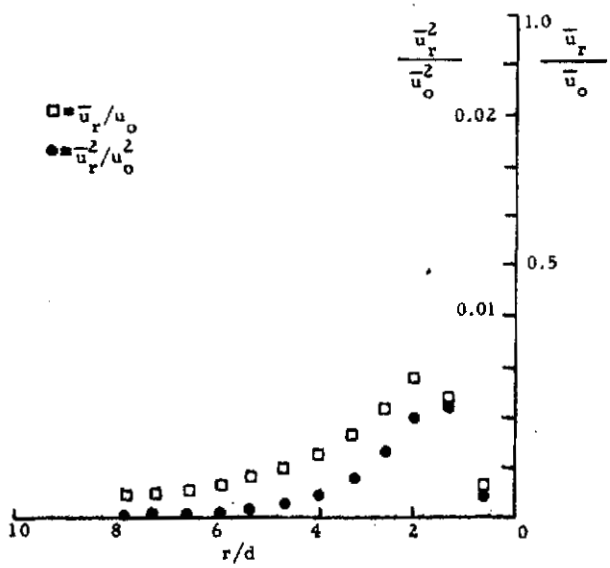

g.) Θ = 135 degrees

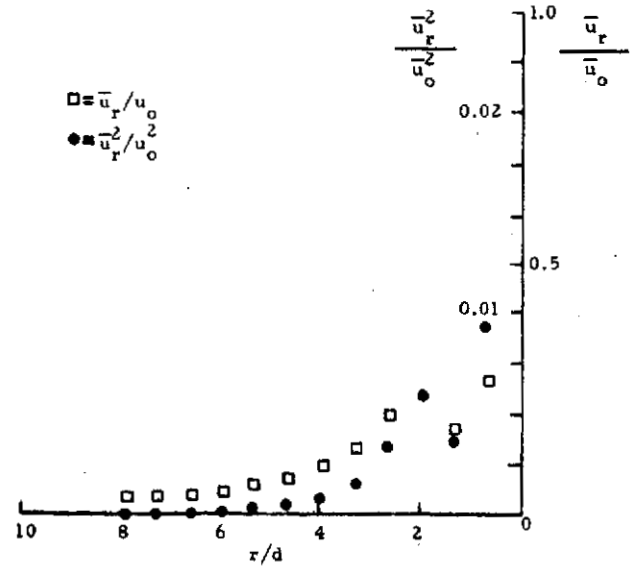

h.) Θ = 180 degrees

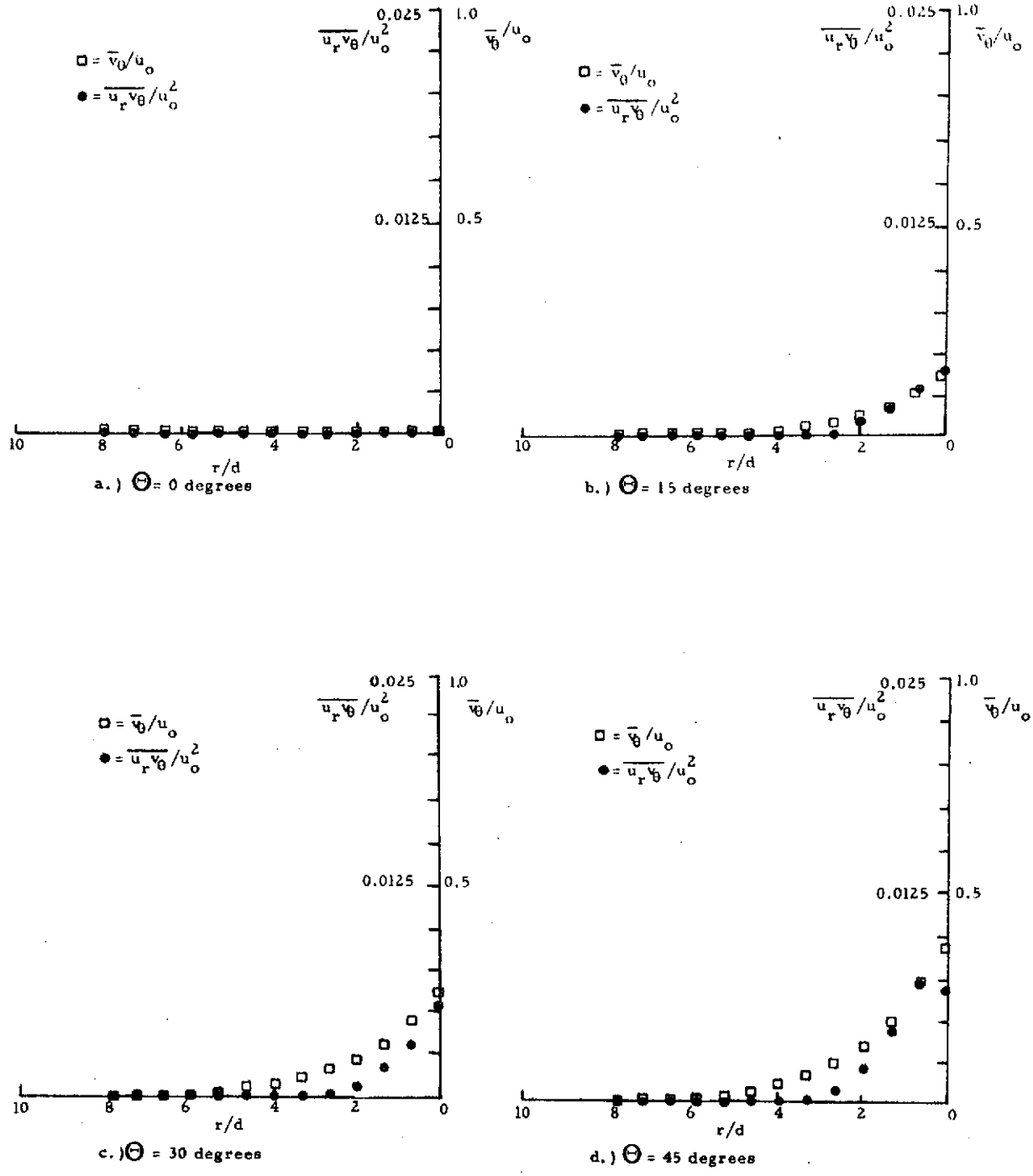

Figure 11. Radial traverses of the azimuthal velocity and the Reynolds shear stress. (Presentation is to allow the magnitude of $\overline{u_r v_\theta}$ $\partial\bar{v}_\theta/\partial r$ to be inferred.)

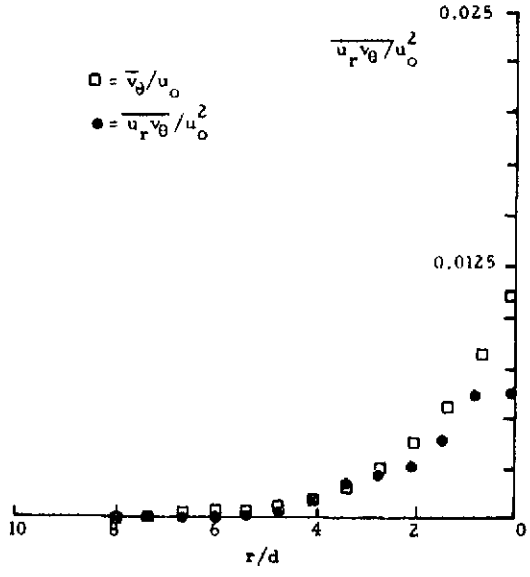

e.) θ = 60 degrees

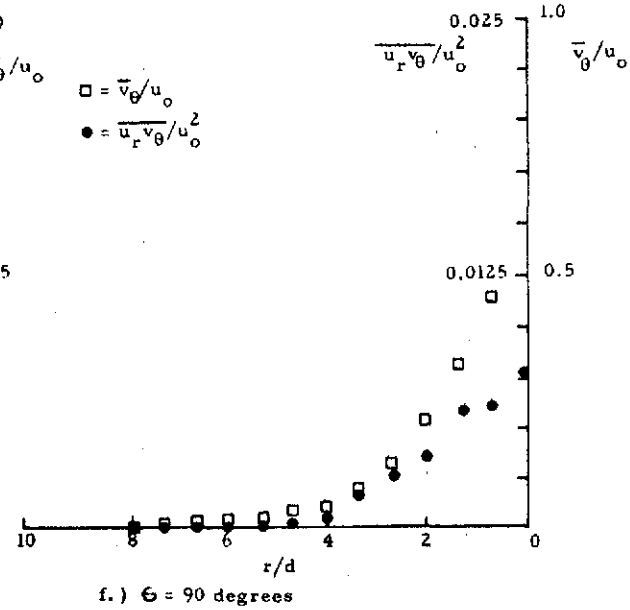

f.) θ = 90 degrees

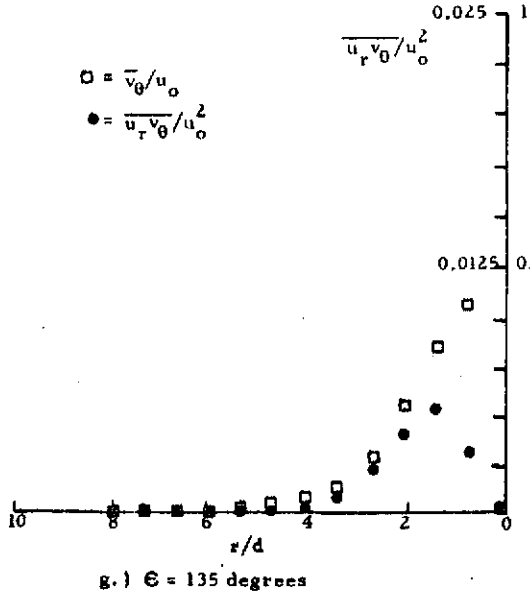

g.) θ = 135 degrees

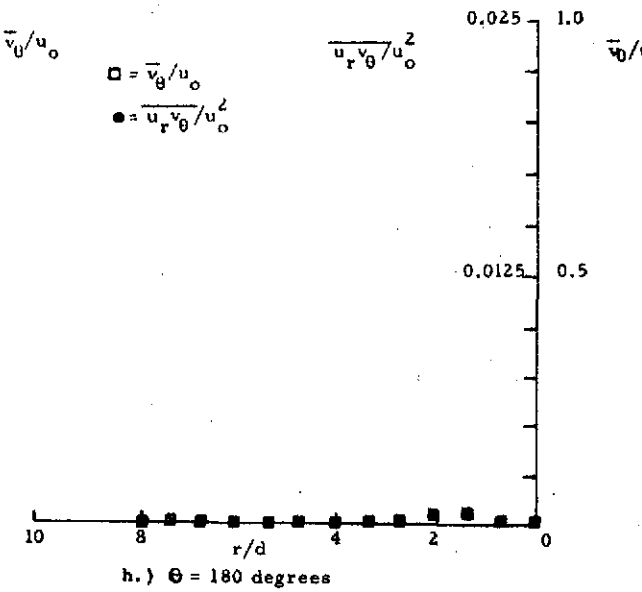

h.) θ = 180 degrees

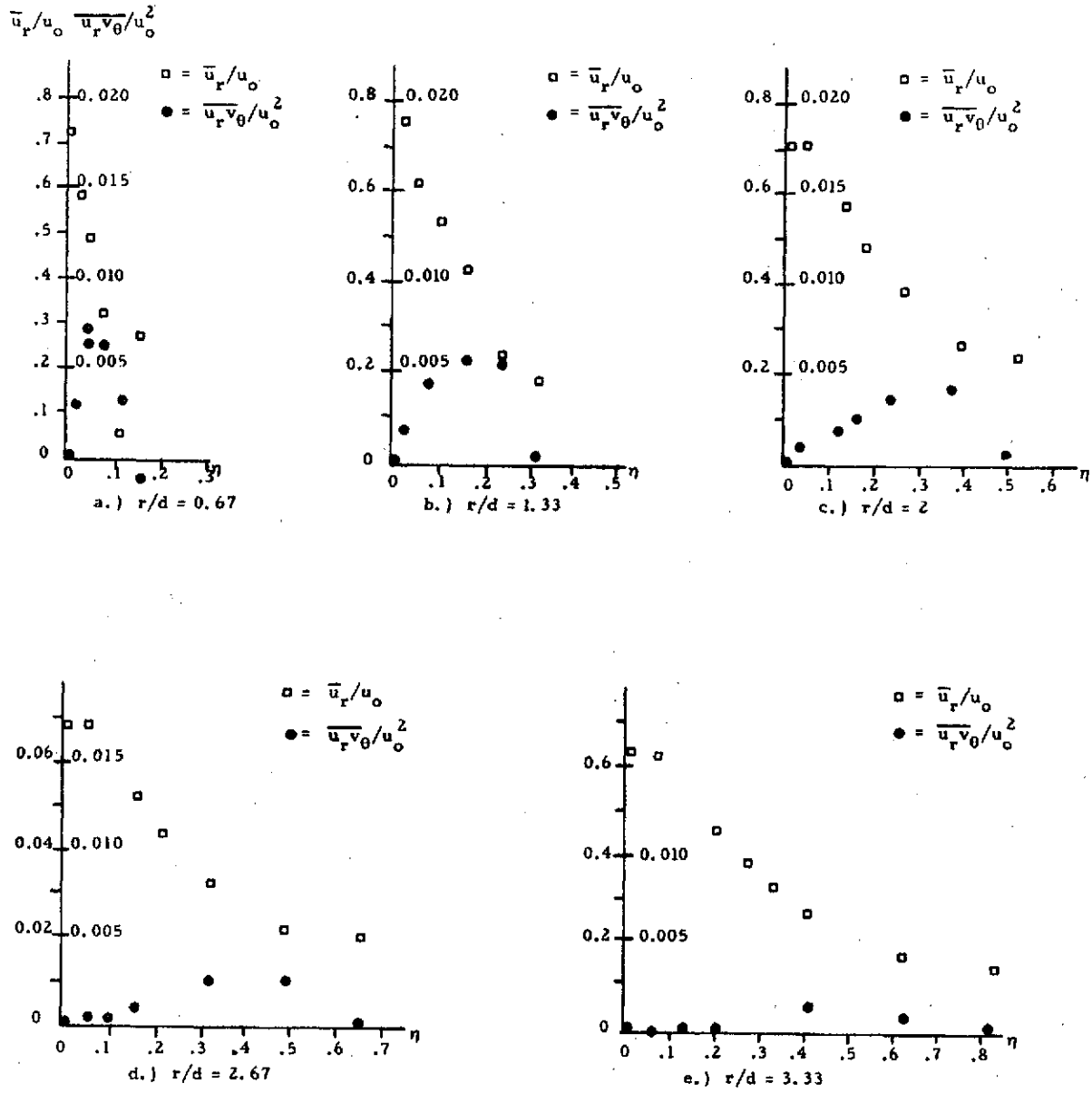

NOTE: The coordinate η ($\eta = [r\theta/d]\ 1[r\theta/d]_{reference}$) is arbitrarily defined such that $r\theta/d_{reference} = 4\pi$

Figure 12. Azimuthal distributions of the radial velocity and Reynolds shear stress. (Presentation is to allow the magnitude of $\overline{u_r v_\theta}\ \partial\bar{u}_r/\partial\, r\theta$ to be inferred)

$\overline{u}_r/u_o$ $\overline{u_r v_\theta}/u_o^2$

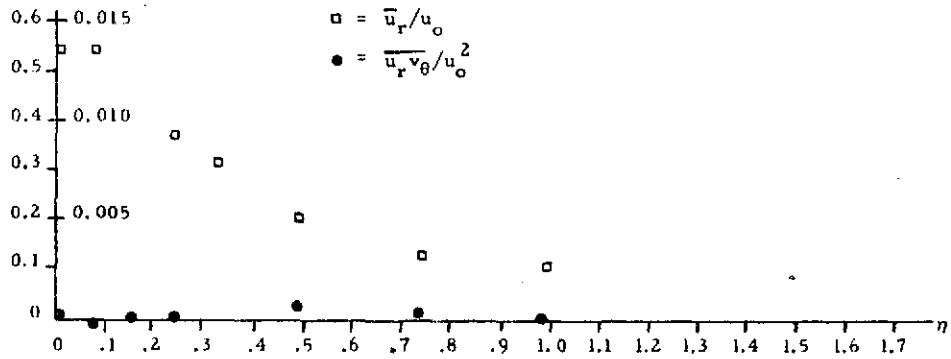

f.) r/d = 4.0

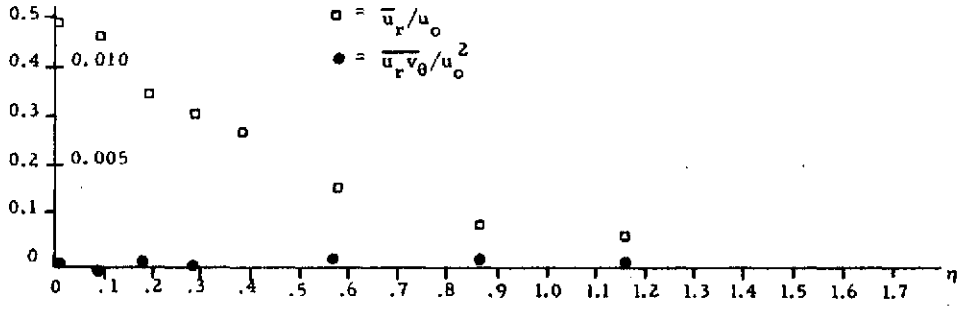

g.) r/d = 4.67

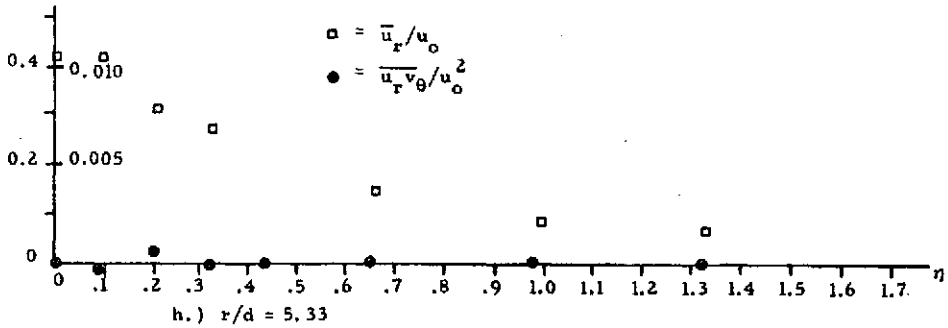

h.) r/d = 5.33

$\overline{u}_r/u_o$ $\overline{u_r v_\theta}/u_o^2$

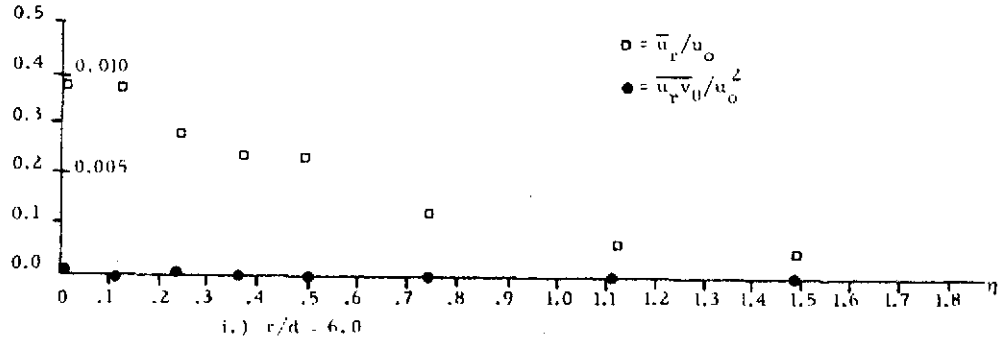

i.) r/d = 6.0

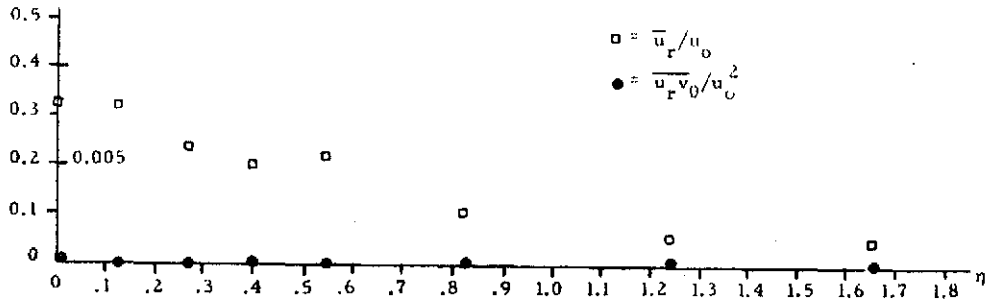

j.) r/d = 6.67

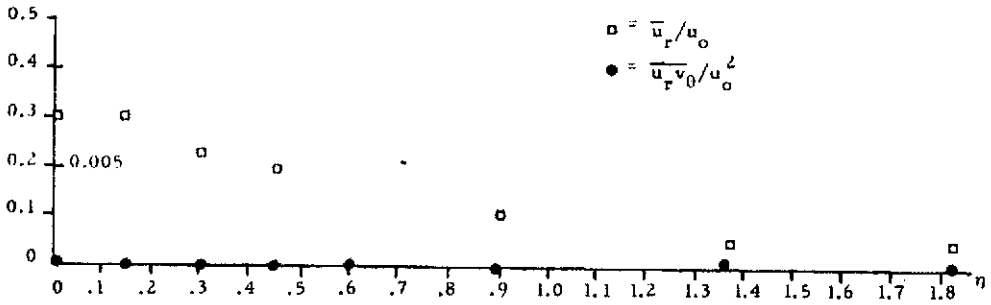

k.) r/d = 7.33

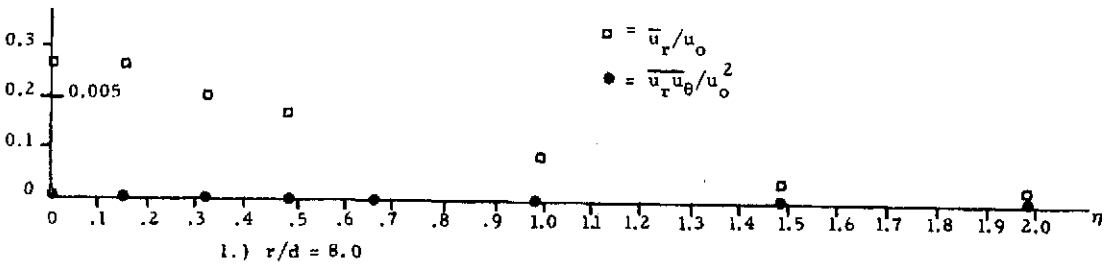

l.) r/d = 8.0

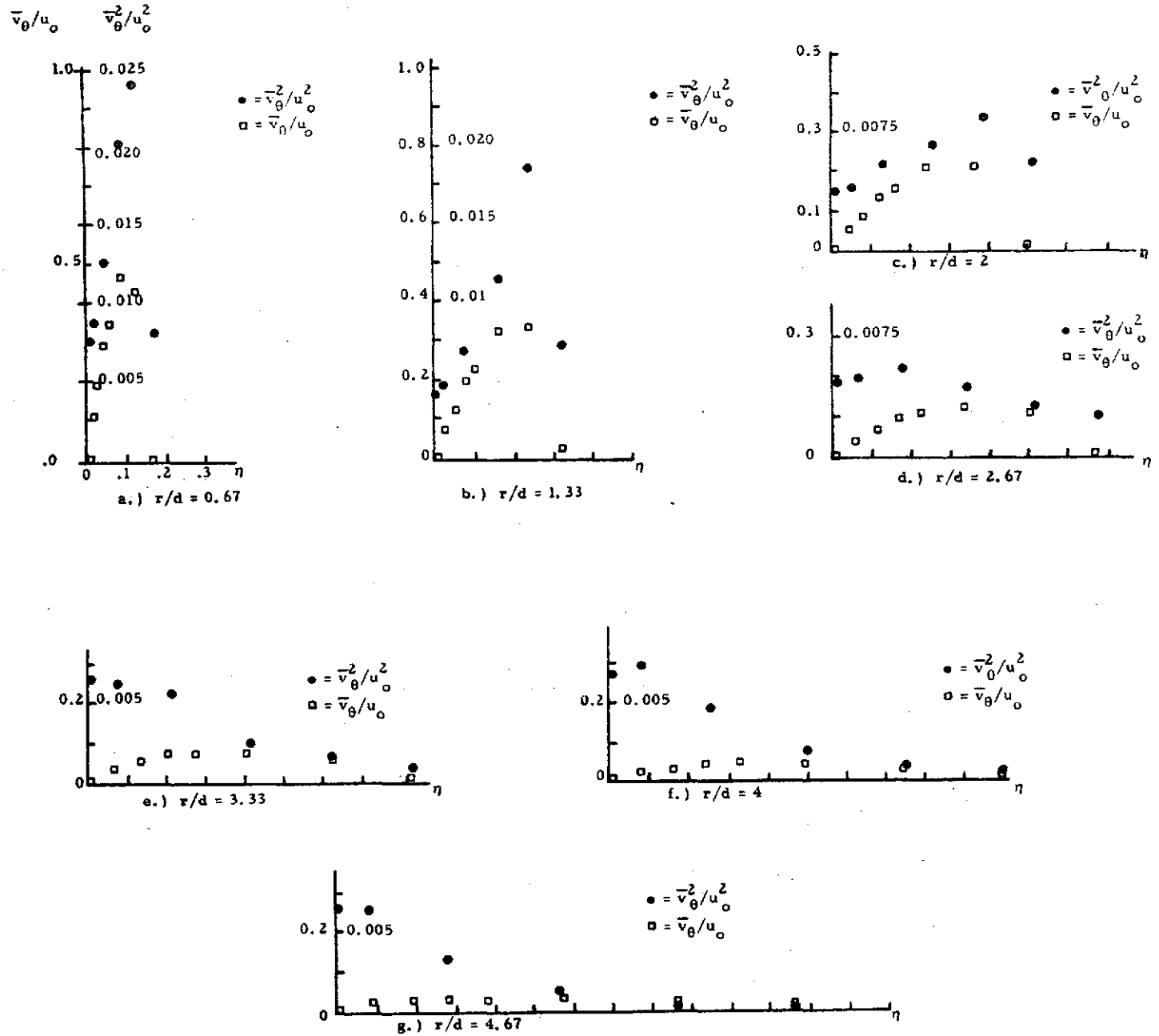

Figure 13. Azimuthal distributions of the azimuthal velocity and the azimuthal Reynolds stress. (Presentation is to allow the magnitude of $\overline{v}_\theta \; \partial \overline{v}_\theta / \partial \, r\theta$ to be inferred.)

Note: The coordinate η ($\eta \equiv [r\theta/d] / [r\theta/d]_{\text{reference}}$) is arbitrarily defined such that $[r\theta/d]_{\text{reference}} = 4\pi$.

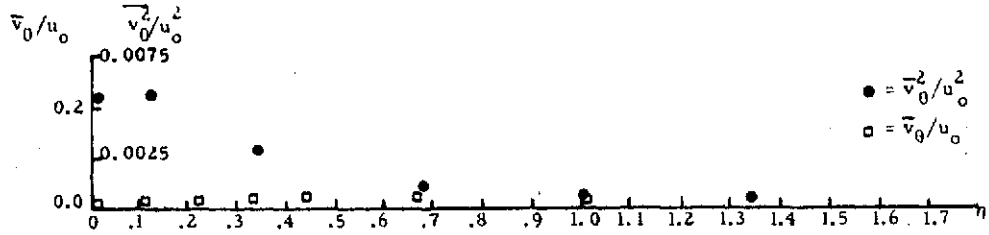

h.) r/d = 5.33

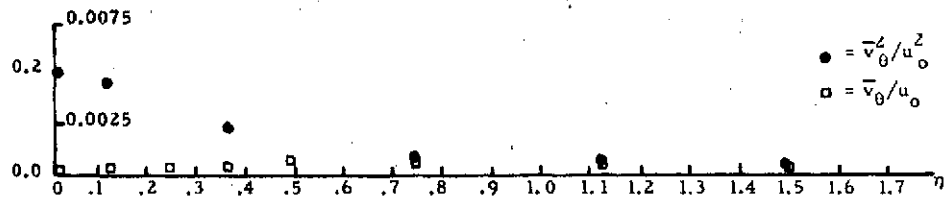

i.) r/d = 6.0

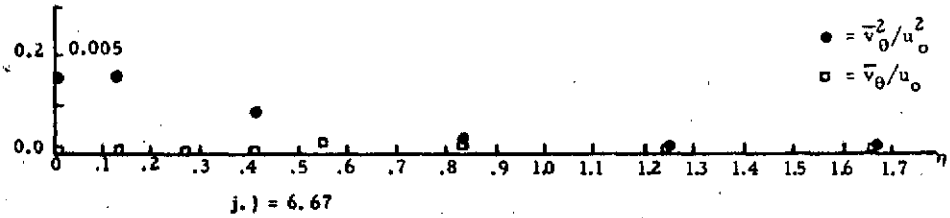

j.) = 6.67

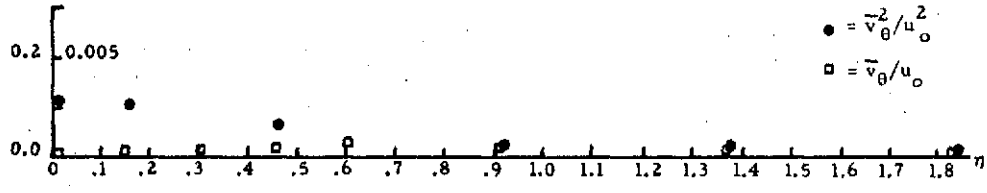

k.) r/d = 7.33

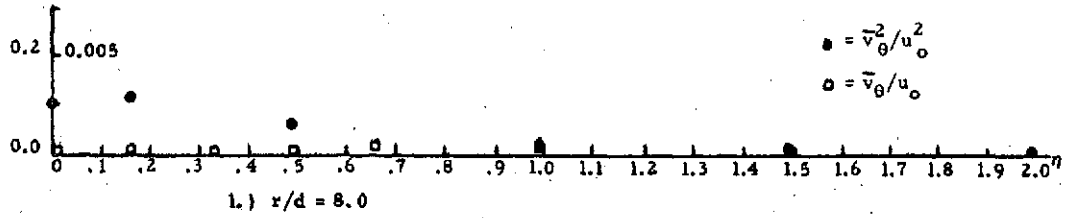

l.) r/d = 8.0

NOTE: The coordinate η ($\eta = [r\theta/d] / [r\theta/d]_{reference}$) is arbitrarily defined such that $r\theta/d_{reference} = 4\pi$

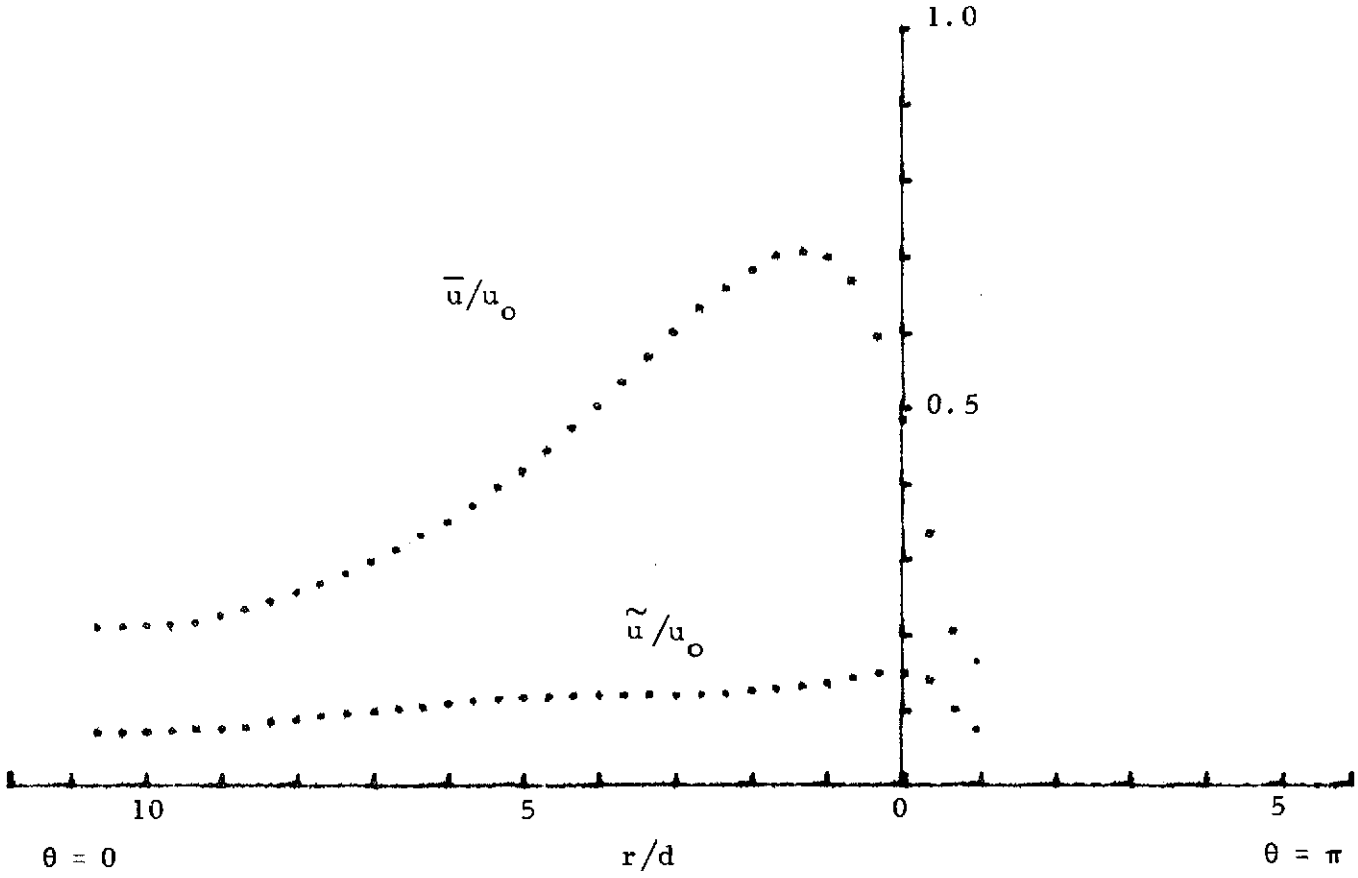

Figure 14. $\overline{u}/u_o$ and $\tilde{u}/u_o$ vs r/d for the θ = 0 plane, z/d = 0.04 (h/d = 7, jet Reynolds number = $u_o d/\nu = 4.8 \times 10^4$).

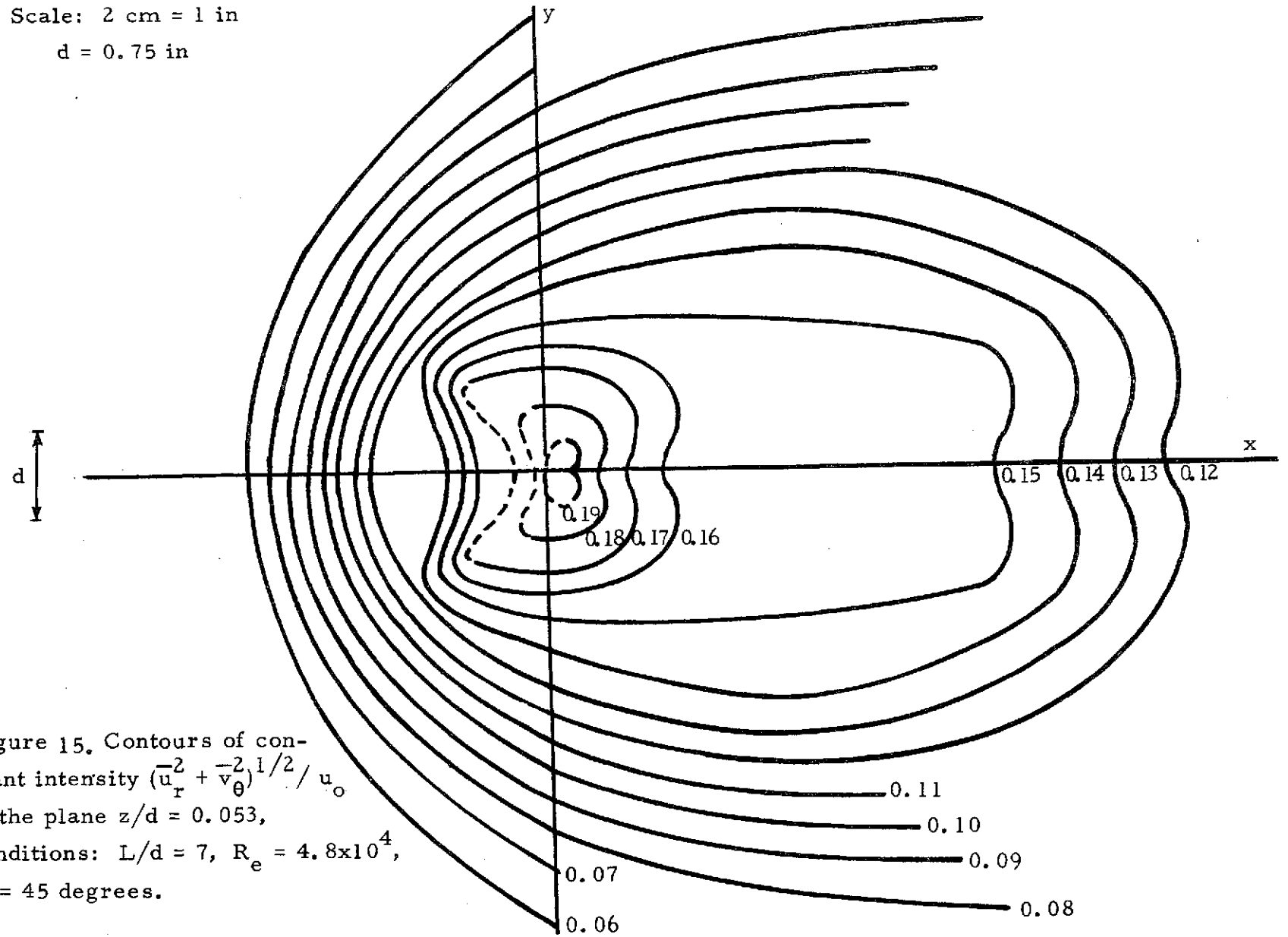

Figure 15. Contours of constant intensity $(\overline{u_r^2} + \overline{v_\theta^2})^{1/2} / u_o$ in the plane $z/d = 0.053$, conditions: $L/d = 7$, $R_e = 4.8 \times 10^4$, $\alpha = 45$ degrees.

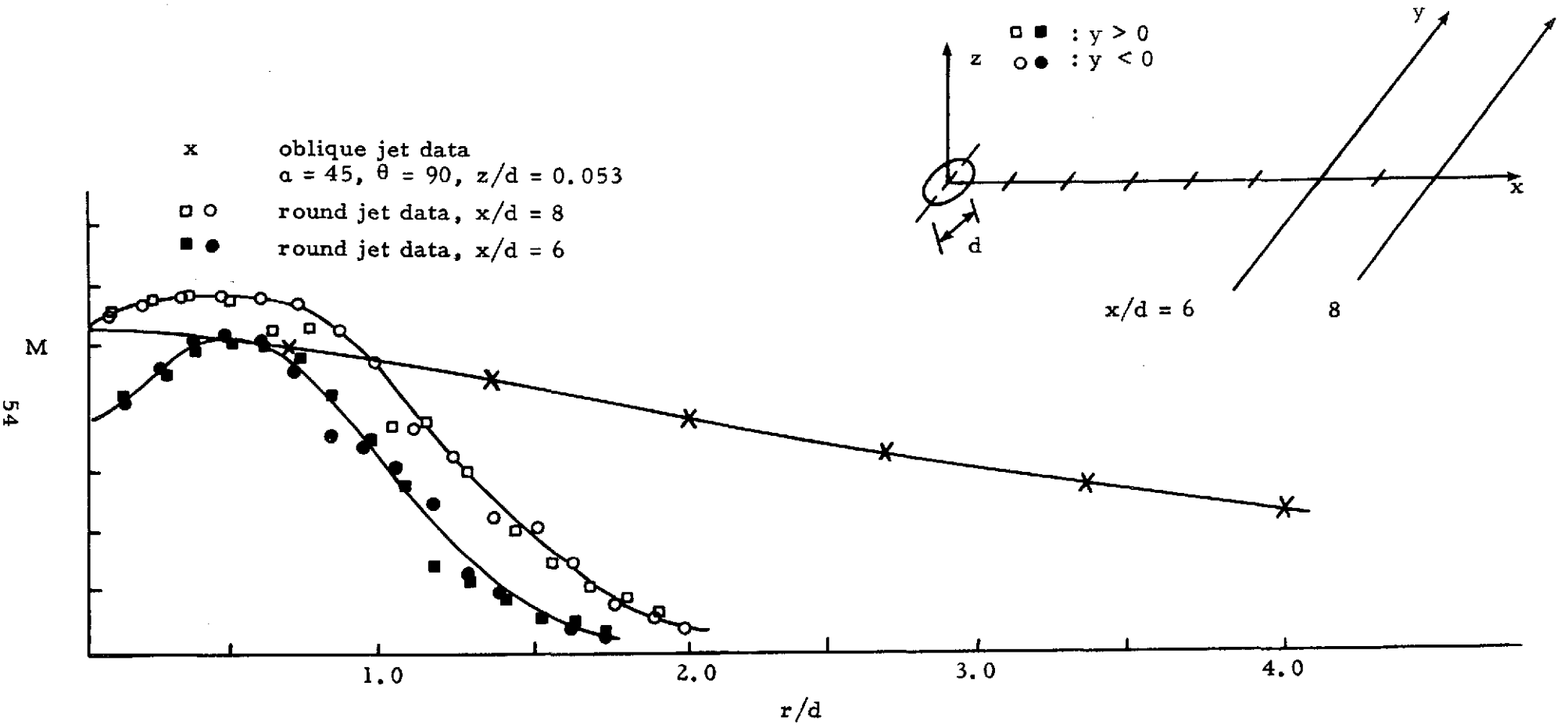

Figure 16. Comparison of turbulence intensity magnitudues from a free and the impinging jet flows. Note $M = (\sqrt{\overline{u^2}} + \sqrt{\overline{v^2}})/u_o$ for the free jet and $(\sqrt{\overline{u_r^2}} + \sqrt{\overline{v_\theta^2}}/\ u_o$ for the oblique impingement flow.

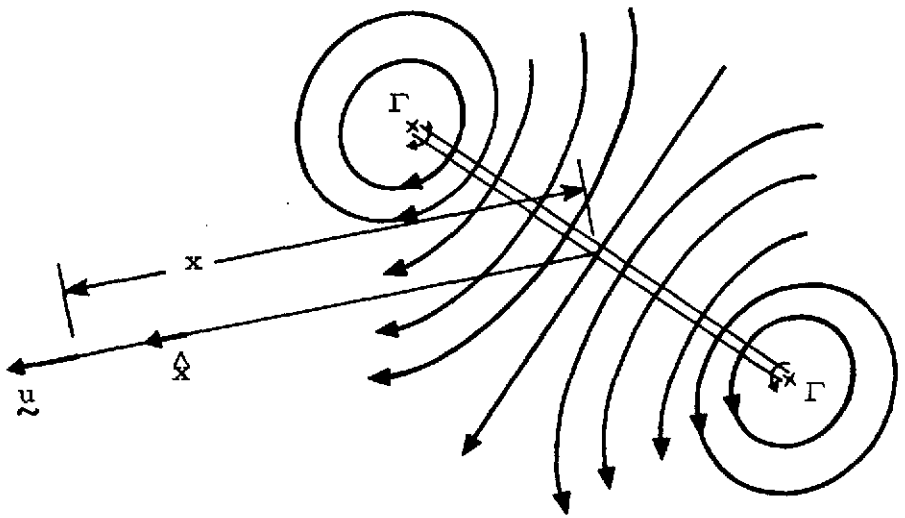

(a) Streamline flow pattern based upon vortex loop with strength Γ.

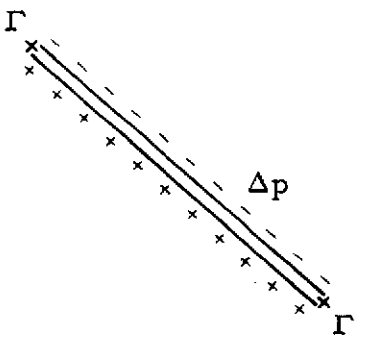

(b) Dipole sheet adjusted to yield the same flow field as in (a).

Figure 17. Terminology for Powell's vortex sound analysis. (Adapted from Figure 3 of [12].)

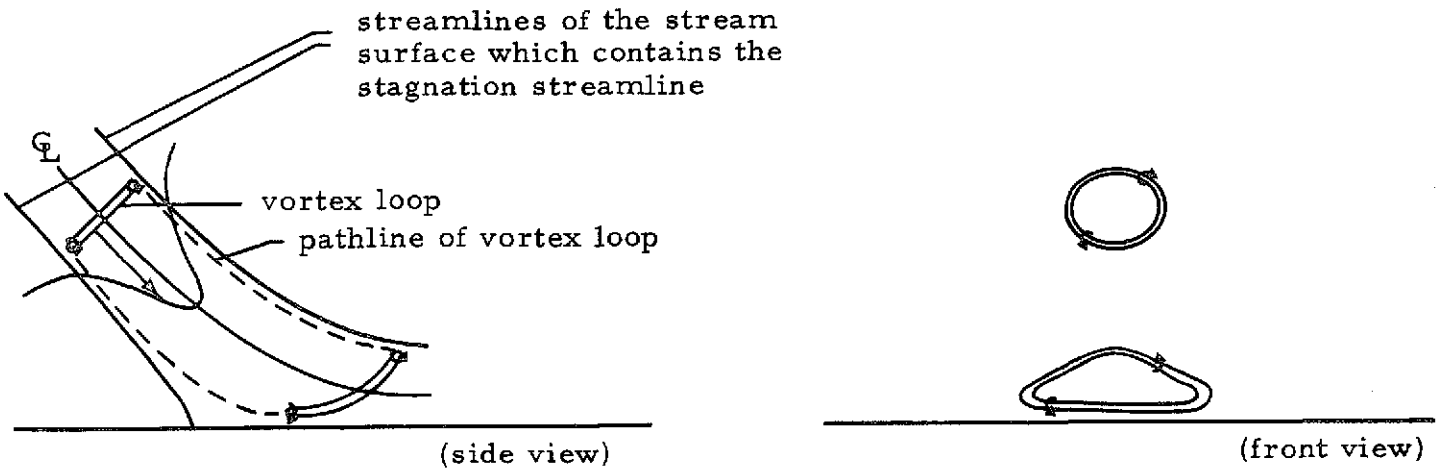

(a) Vortex loop stretching "inside" the stagnation streamline.

(b) Vortex loop exterior to the stagnation streamline which is reconstituted as a result of the surface vorticity flux.

Figure 18. Schematic representation of vortex loop behavior which contributes to the quantity $d^2(\Gamma s)/dt^2$.